Deformation processes adjacent to active faults: Examples from eastern California

Eitan Shelef[1] and Michael Oskin[2]

[1]   Major seismogenic faults are embedded within narrow zones of inelastic off-fault deformation (OFD), where both distributed displacement and modification of rock properties occur. Active distributed displacement may affect slip rate estimates, seismic energy radiation and geodynamic models. This study addresses the role of OFD in the displacement history and mechanical behavior of seismogenic faults, by multisite study of deformed geologic features adjacent to 30–60 km long active strike-slip faults of <10 km of dextral displacement in the Mojave Desert, eastern California. We find that distributed displacement accommodates 0 to ~25% of the total displacement over zones of one to two kilometers width. Displacement occurs mostly within 100–200 m of faults and decreases nonlinearly away from the main fault. We show evidence for distributed displacement through simple shear in the form of parallel secondary faults and progressive deformation of linear markers adjacent to the Calico fault. We also find evidence for shear via rotation and progressive fragmentation adjacent to the Harper Lake fault. Analysis of block dimensions show that blocks tend to decrease in size toward faults and that cumulative length of secondary faults is longer than the main fault by at least a factor of 10. Based on crosscutting relationships and the relationship of OFD to geophysically imaged compliant zones around active faults, we argue that distributed displacement is an active process and suggest that zones of diminished rigidity near faults may be at least in part driven by secondary faulting during the rupture propagation along the main fault.

1.   Introduction

[2] Major seismogenic faults occur within bands of inelastic off-fault deformation (OFD), where, in the broadest sense, deformation includes both distributed shear displacement and modification of rock properties through fracture damage [*Li et al.*, 1998; *Fialko et al.*, 2002; *Katz et al.*, 2003; *Faulkner et al.*, 2006]. In the brittle crust, OFD includes faulting, rigid body rotation and fracturing (Figure 1) [*Nelson and Jones*, 1987; *Sonder et al.*, 1994; *Katz et al.*, 2003]. Distributed shear displacement within OFD zones along strike-slip faults can account for up to 60% of the total displacement across a fault zone [*Nelson and Jones*, 1987; *Miller and Yount*, 2002; *Kimurah et al.*, 2004]. This distributed displacement is difficult to observe and quantify and thus is often ignored in tectonic reconstructions. If distributed displacement is the result of an ongoing and active process, it will change slip rate estimates and thus could

affect comparisons with geodetic loading rates, seismic hazard analysis, and geodynamic models [*Thatcher and Lisowski*, 1987; *Salyards et al.*, 1992; *Hilley et al.*, 2005]. Coseismic fracturing in the rock mass surrounding an active fault also represents a potentially significant sink of seismic energy [*Wilson et al.*, 2005; *Chester et al.*, 2005; *Shipton et al.*, 2006].

[3] By modifying bulk rock properties, OFD plays an important role in the mechanics of faulting. OFD leads to a reduction of shear rigidity within the fault zone that affects stress orientation and elastic strain distribution next to faults [*Faulkner et al.*, 2006]. In detail, this process involves the accumulation of damage through creation and growth of cracks in a rock mass [*Scholz et al.*, 1993; *Vermilye and Scholz*, 1998; *Li et al.*, 1998, 2002, 2003; *Yamashita*, 2000; *Lemaitre and Desmorat*, 2005]. Compliant fault zones (i.e., zones of reduced shear rigidity) have been observed seismically and geodetically [*Li et al.*, 1998; *Li and Vidale*, 2001; *Fialko et al.*, 2002; *Fialko*, 2004; *Cochran et al.*, 2009] and are attributed to damage acquired during coseismic dynamic rupture propagation [*Li et al.*, 1998, 2002, 2003; *Yamashita*, 2000].

[4] Distributed shear displacement is usually quantified from deflected planar and linear features next to faults

[1]Department of Geological and Environmental Sciences, Stanford University, Stanford, California, USA.
[2]Department of Geology, University of California, Davis, California, USA.
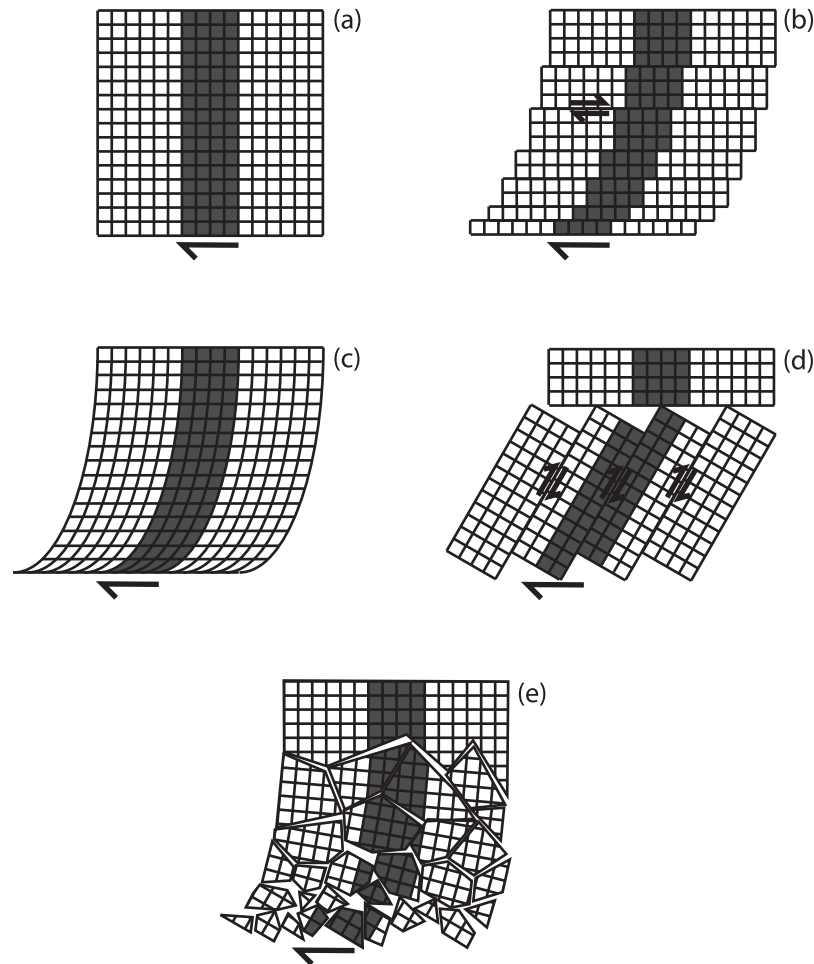
Figure 1. Mechanisms of off-fault displacement, redrafted from *Nelson and Jones* [1987]. (a) Undeformed domain, (b) shear on faults sub parallel to the main fault, (c) pervasive continuous shear, (d) block rotation accompanied by internal antithetic shear, and (e) small block rotation.

[*Albers*, 1967; *Thatcher and Lisowski*, 1987; *Nelson and Jones*, 1987; *Richard et al.*, 1991; *Sonder et al.*, 1994; *Miller and Yount*, 2002; *Katz et al.*, 2003; *Kimurah et al.*, 2004]. Resolution of displacement patterns associated with these features depends on scale of observation and may appear continuous. The convex shape of continuously deflected geologic features next to faults is often called "fault drag" [*Dennis*, 1972; *Reches and Eidelman*, 1995], "drag folds" [*Davis*, 1984], or "flanking features" [*Passchier*, 2001].

[5] This study addresses the role of OFD in the displacement history and mechanical behavior of major seismogenic faults, and focuses on the component of OFD expressed as distributed shear displacement. We characterize attributes of distributed displacement from geologic field observations. These characteristics include quantifying: (1) The fraction of the total shear displacement that occurs as distributed displacement, (2) the width of the distributed displacement zone, (3) the distribution of displacement within this zone. We also address the questions of the activity of distributed displacement, what structural mechanisms accommodate this displacement, and how distributed

displacement is related to compliant zones surrounding active faults.

[6] To determine the role of OFD along active strike-slip faults field studies were conducted in the Mojave Desert of southern California. The Mojave section of the eastern California shear zone (ECSZ, Figure 2), has been an area of active strike-slip faulting since the early Miocene [*Glazner et al.*, 2002] and is traversed by a set of 30–60 km long dextral faults. The potential discrepancy between fast geodetic rates [*Dixon et al.*, 1995; *Gan et al.*, 2000; *Miller et al.*, 2001; *Bennett et al.*, 2003; *Meade and Hager*, 2005] to slow fault slip rates across the ECSZ [*Rockwell et al.*, 2000; *Oskin et al.*, 2008] may be at least in part due to unaccounted distributed displacement. Abundant exposures of planar and linear features surrounding active faults in the Mojave Desert provide ample opportunity to study the magnitude, mechanism and activity of distributed displacement. Well-documented $M_W > 7$ earthquakes that occurred in the Mojave Desert in 1992 and 1999 led to observations of coseismic patterns of OFD [*Johnson et al.*, 1994; *Michel and Avouac*, 2006; *McGill and Rubin*, 1999; *Treiman et al.*, 2002]. These patterns can be compared with distributed
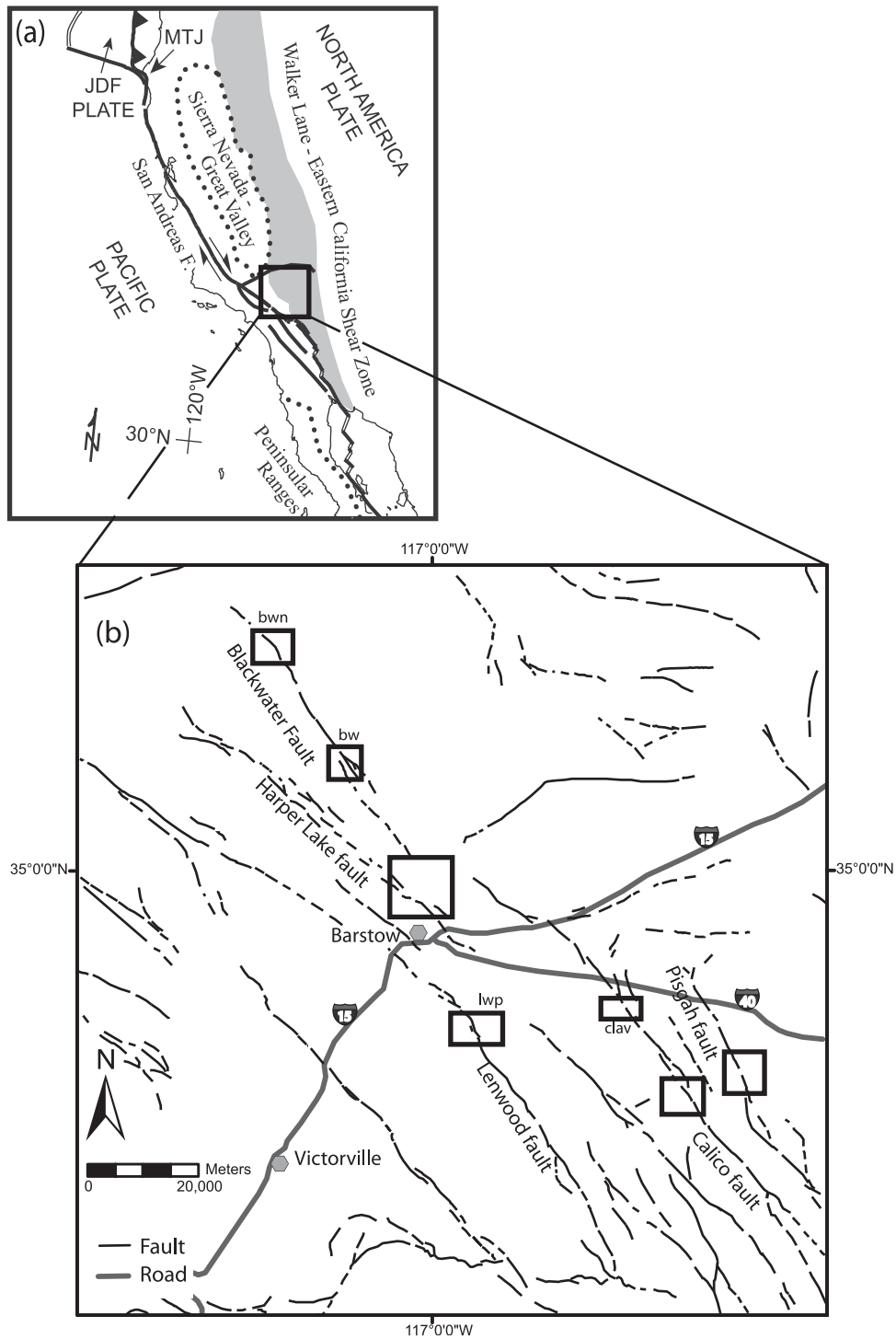
Figure 2. (a) Index map of the Eastern California Shear Zone (ECSZ) [from *Oskin and Irondio*, 2004]. (b)The Mojave Desert section of the ECSZ, black boxes show study areas adjacent to active dextral faults. Paleomagnetic study sites: lwp, Lenwood fault; bw, blackwater fault south; bwn, blackwater fault north; clav, Calico fault at Kane Wash.

displacement integrated over multiple seismic cycles as recorded by geologic features.

[7] In this paper, we focus on macroscopic planar and linear geologic features next to faults that record net shear displacement by faulting and rotation. We first present observations from the Calico fault that show distributed displacement of continuous, unique planar markers such as faults and dikes. This is followed by observations of distributed displacement via rotation recorded by local linear markers such as mylonitic lineation, measured next
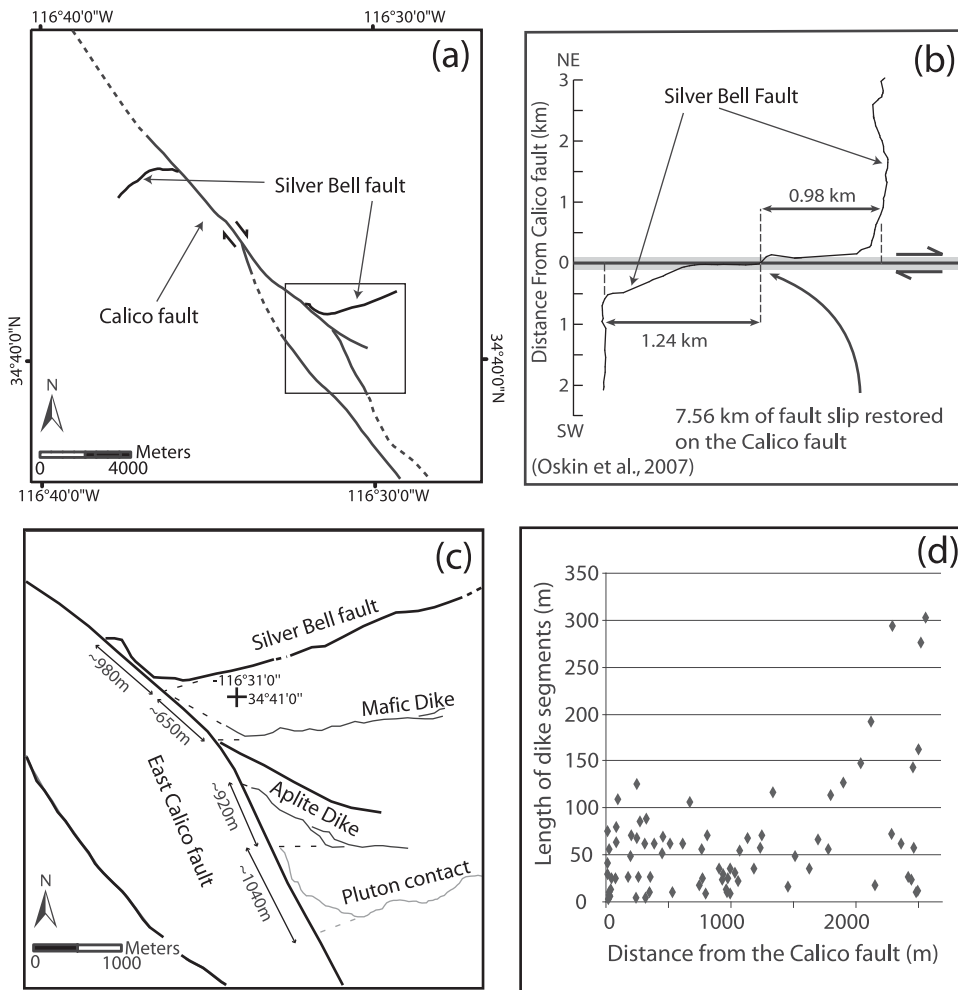
Figure 3. Deflected geologic features next to the Calico fault. (a) Fault lines in the central portion of the Calico fault [after *Dibblee*, 1964a, 1964b]. Note the deflection of the Silver Bell fault as it approaches the Calico fault. (b) The deflected form of the Silver Bell fault [after *Glazner et al.*, 2000; *Oskin et al.*, 2007]. (c) Inset map of deflected dikes, fault, and contact within the framed area at Figure 3a. (d) Lengths of dike segments versus distance from the Calico fault as measured with differential GPS (horizontal location error < 1 m) along dikes shown at Figure 3c (mostly along the mafic dike). Note the increase in segment length at 1500–2000 m from the fault.

to the Harper Lake fault, and paleomagnetic vectors, measured next to the Calico, Lenwood, and Blackwater faults. Observations are then analyzed to quantify the characteristics of OFD and results are discussed in the comparative framework of this multisite study. The discussion also includes comparison between patterns of distributed displacement, and those of fault compliant zones [*Li et al.*, 1998, 2003; *Li and Vidale*, 2001; *Fialko et al.*, 2002; *Fialko*, 2004; *Cochran et al.*, 2003] and of coseismic surface ruptures [*Johnson et al.*, 1994; *Michel and Avouac*, 2006; *McGill and Rubin*, 1999; *Treiman et al.*, 2002].

2. Observations

2.1. Deflection of Continuous Planar Markers Within OFD Zones

[8] Continuous, formerly planar markers oriented at high angle to a fault provide the most complete picture of dis-

tributed displacement. Such markers record total magnitude of shear displacement, patterns of faulting and rigid body rotation, width of the OFD zone, and the distribution of shear displacement within this zone. Figure 3 shows dikes and faults that are deflected as they approach the crosscutting Calico fault. The convex shape of a set of Mesozoic aplite dikes indicates distributed shear displacement of ~650 to ~1040 m and suggests that distributed displacement increases nonlinearly toward the fault. A few kilometers to the north, *Dokka* [1983] and *Glazner et al.* [2000] found a similar deflection of the west striking Miocene Silver Bell fault as it approaches the Calico fault (Figure 3). *Oskin et al.* [2007] show that the deflection of this fault increases nonlinearly such that 70% of distributed displacement occurs within 100 m of the Calico fault.

[9] Detailed mapping of a set of mafic dikes located between these deflected markers and next to the Calico fault further illustrates how shear displacement is accomplished
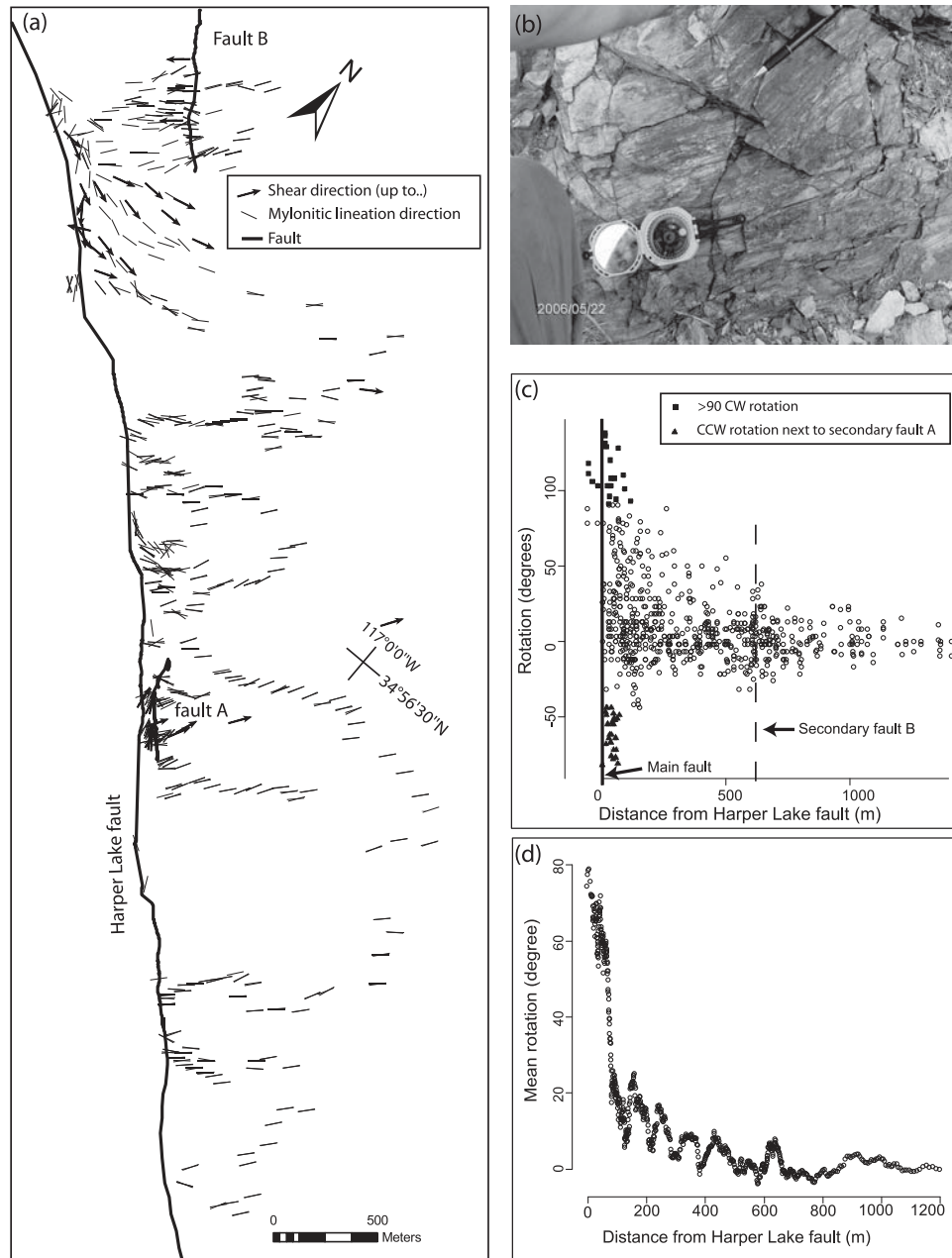
Figure 4. Mylonitic lineation measurements along the Harper Lake fault. (a) Mylonitic lineation measurements along the Harper Lake fault. Short gray lines represent measurements of mylonitic lineation azimuth, black arrows represent shear direction of the upper plate based on kinematic indicators, where measured. Faults A and B are mapped segments of the secondary faults shown in Figures 5 and 8. The few mylonitic lineations west of the Harper Lake fault are due to an isolated metamorphic rock outcrop at this side of the fault. Note that kinematic indicators show a shear sense of southeast west of secondary fault B and north-northwest just west of secondary fault A. (b) Field exposure of mylonitic lineation. The picture shows change in mylonitic lineation direction across a fault, due to brittle deformation that postdates mylonitization. (c) Azimuthal component of mylonite rotation versus distance from the Harper Lake fault (n = 733, horizontal location error <15 m). Rotation values are stacked along all 6.5 km of fault strike. Rotation was calculated relative to the farthest point from the fault. Negative rotation values indicate CCW rotation. We used kinematic indicators next to key areas of high rotation values to interpret >90°CW rotation (solid squares) and large CCW rotations (solid triangles). Note the area of approximately homogenous rotation values between 800 and 1500 m from the fault. (d) Running average over 30 measurement points show a trend of increasing clockwise rotation toward the fault.
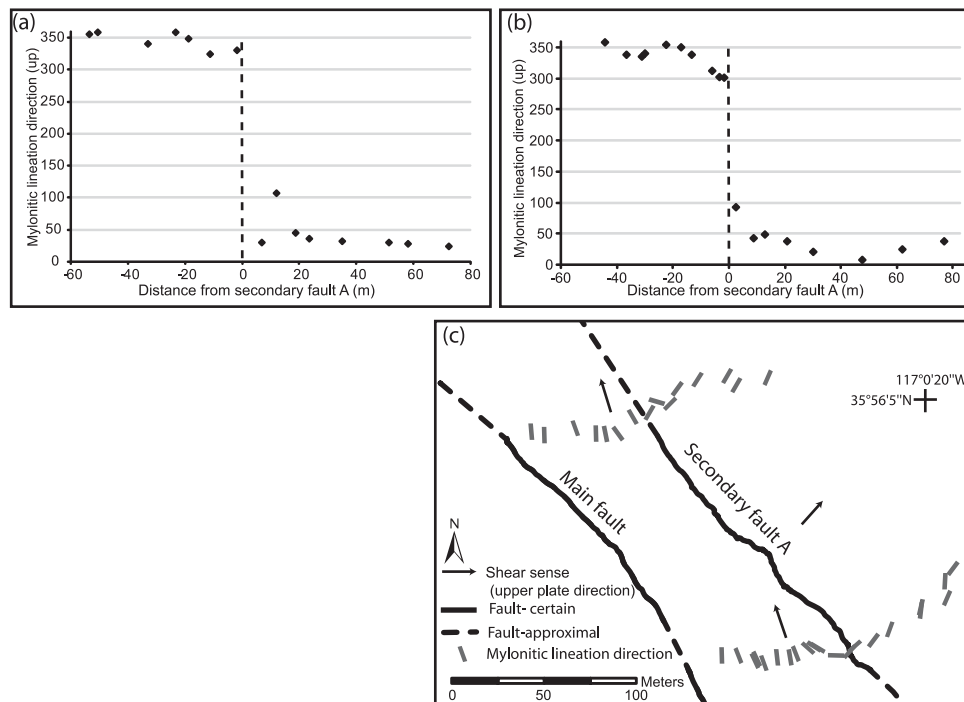
Figure 5. Azimuthal component of Mylonite lineation versus distance from secondary faults adjacent to the Harper Lake fault. Secondary fault and mylonitic lineation measurements were located with differential GPS. (a and b) Azimuthal component of Mylonite lineation along two fault-normal transects (n = 33, horizontal position error <1 m). The direction of the lineation vector is interpreted from nearby kinematic indicators. (c) Map view of the two transects, Figure 5a is the northern transect, Figure 5b is the southern transect.

within OFD zones. The dikes are contained within homogeneous, but pervasively fractured quartz monzonite. Segmentation of the dikes illuminates the spacing of small faults that would otherwise be difficult to observe. Mapping of dike segments using differential GPS (horizontal location error < 1 m) shows that the length of dike segments decreases toward the fault (Figure 3d). In some cases, dike segments are separated by conjugate sinistral and dextral faults. Other boundaries may be due to segmentation during dike intrusion [*Baer and Reches*, 1991] and thus unrelated to OFD.

2.2. Rotation of Local Linear Markers Within OFD Zones

[10] Unlike continuous markers, local linear markers, such as mylonitic lineation and paleomagnetic remanent direction, measure only a component of OFD via rotation. These measurements give insight into the mechanism of block rotation, the width of OFD zones, and the distribution and magnitude of displacement via rotation.

[11] Orientations of mylonitic lineations in the early Miocene central Mojave metamorphic core complex [*Fletcher et al.*, 1995] exposed in the Mitchel Range (Figures 4a, 4b, and 4d) show that on average the trends of mylonitic lineations are deflected clockwise approaching the Harper Lake fault (Figures 4c and 4d). We observe that this rotation is accommodated by brittle fragmentation of the mylonitic rocks and is unrelated to the ductile mylonite fabric. The mylonitic fabric itself was formed earlier and exhumed by

NE directed extension prior to the onset of NW directed strike-slip faulting. Essentially the mylonitic fabric serves as a passive marker of later, brittle OFD along the Harper Lake fault. The amount and character of rotation of the mylonitic lineation fabric varies along fault strike. Observations (n = 733, see auxiliary material) show increasing mean and variance of the azimuthal component of rotation values toward the fault (Figure 4).[1] Although some upright folding along an axis parallel to the Harper Lake fault has been mapped [*Fletcher et al.*, 1995], mylonite orientation appear not to be significantly affected by tilting about such axis. Thus, the azimuthal component of mylonite rotation predominantly records vertical axis rotation.

[12] Mylonitic lineation data also show that rotation occurs adjacent to secondary faults. Measurements along two transect lines (n = 33) across a ~1.5 km long secondary dextral fault (fault A, Figure 4a) show continuous rotation. Interpretation of shear sense indicators measured on both sides of secondary fault A suggests that block rotation about vertical axis exceeds 90° (Figure 5). Rotation starts 20–30 m from this fault and is approximately symmetric across it.

[13] We used paleomagnetism to measure block rotation next to faults at four different sites. These areas differ by parameters such as the time of emplacement of the sampled unit, the underlying lithology and fault structure (Figures 2

---

[1]Auxiliary materials are available at ftp://ftp.agu.org/apend/jb/2009jb006289.
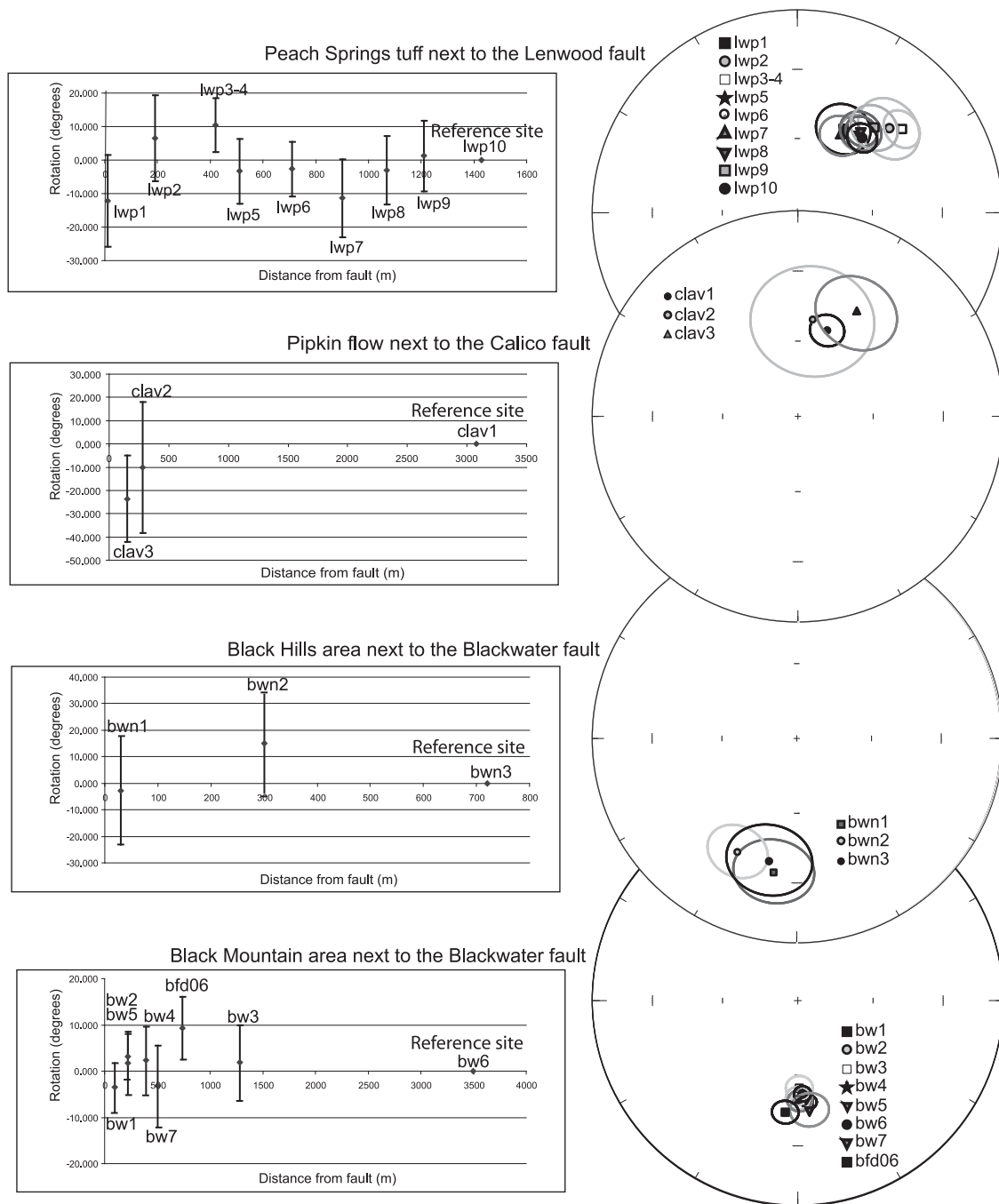
Figure 6. Scatterplots show rotation values for paleomagnetic sites next to the Calico, Blackwater and Lenwood faults. Equal area plots show the actual declination and inclination values for each site, as well as the $\alpha 95$ confidence limit around site mean. See Figure 2 and Table 1 for site locations. Rotation values are calculated relative to the furthest measurement site from the fault. Negative rotation values indicate counterclockwise rotation. Rotation errors are calculated according to *Demarest* [1983].

and 6, Table 1). Each area is composed of 3 to 10 sampling sites located at increasing distances from a fault. Most sites consist of 6–10 individual samples collected over an area of 10 to 50 m^2. All core samples were oriented in situ using both magnetic and solar compasses. Demagnetization measurements were carried with a superconducting cryogenic magnetometer sensitive to 2×10^{-9} emu. Most samples underwent alternating field demagnetization up to 70 mT,

with 5 mT steps up to 10 mT, and 10 mT steps between 10 to 70 mT. Specimens from cores of samples that did not yield stable primary magnetization went through demagnetization path composed of alternating field demagnetization of 2.5 mT steps between 2.5 mT to 10 mT, followed by thermal steps of 50°C from 150° to 650°C. Line and plane fits were calculated following *Kirschvink* [1980], site mean directions and $\alpha 95$ were calculated [*Fisher*, 1953], and tilt

Table 1. Paleomagnetic Data[a]

Lithologic Unit	Site	Distance From Fault (m)	Age (Ma)	Declination (deg)	Inclination (deg)	α95	k	n/n₀	Rotation (deg)	Rotation Error (deg)	Flattening (deg)	Flattening Error (deg)	Latitude (deg)	Longitude (deg)	Tilt Correction Strike	Tilt Correction Dip
Pipkin Basalt	clav1	3080	0.77 ± 0.04[b]	18.8	53.6	6.7	163.7	7/7	Reference Site	Reference Site	Reference Site	Reference Site	34.7586	−116.65441	None	None
	clav2	280	0.77 ± 0.04[b]	8.7	50.4	23.2	16.6	6/6	−10.1	28.1	−3.2	17.0	34.7775	−116.63398	None	None
	clav3	140	0.77 ± 0.04[b]	29.5	41.4	15.3	14.2	7/9	−24.4	17.9	−12.2	12.7	34.7782	−116.63287	None	None
Black Mountain Basalt (unit 3)	bw1	100	3.77 ± 0.11[c]	173.6	−48.8	2.8	403.7	8/8	−3.5	5.3	3.7	3.3	35.1983	−117.19334	None	None
	bw2	220	3.77 ± 0.11[c]	179.8	−50.2	2.3	602.7	7/8	2.7	4.9	2.3	3.0	35.1968	−117.19356	None	None
	bw3	1280	3.77 ± 0.11[c]	179.0	−54.9	5.1	119.7	8/8	1.9	8.1	−2.4	4.7	35.1996	−117.20983	None	None
	bw4	391	3.77 ± 0.11[c]	179.5	−50.8	4.8	160.2	7/8	2.4	7.2	1.7	4.5	35.2049	−117.20252	None	None
	bw5	220	3.77 ± 0.11[c]	178.9	−49.6	4.4	156.0	8/8	1.8	6.7	2.9	4.2	35.2064	−117.20164	None	None
	bw6	3500	3.77 ± 0.11[c]	177.1	−52.5	3.2	301.1	9/9	Reference Site	Reference Site	Reference Site	Reference Site	35.2046	−117.14781	None	None
Black Mountain Basalt (unit 4)	bw7	500	3.77 ± 0.11[c]	173.9	−45.5	7.1	166.2	4/8	−3.2	8.7	7.0	5.9	35.1756	−117.16266	None	None
	bfd06	740	3.74 ± 0.05[c]	186.4	−44.3	4.9	154.6	6/8	9.3	6.7	8.2	4.6	35.1925	−117.17934	314	25
Black Hills Dacite	bwn1	30	7.23 ± 1.07[d]	189.8	−33.9	14.3	23.7	5/8	−2.9	20.2	4.5	16.1	35.3504	−117.30122	247	6
	bwn2	300	7.23 ± 1.07[d]	207.6	−37.4	11.2	81.8	3/3	14.9	18.5	1.0	14.5	35.3555	−117.29589	247	6
	bwn3	720	7.23 ± 1.07[d]	192.7	−38.4	15.5	13.8	7/7	Reference Site	Reference Site	Reference Site	Reference Site	35.3528	−117.29943	247	6
Peach Springs Tuff	lwp1	10	18.5 ± 0.2[e]	28.5	51.1	10.4	47.8	6/6	−12.1	13.7	1.3	14.3	34.7581	−116.92631	70	10
	lwp2	190	18.5 ± 0.2[e]	47.1	38.7	12.1	19.2	9/9	6.5	12.8	−11.1	15.1	34.7588	−116.92431	70	10
	lwp3–4	420	18.5 ± 0.2[e]	51.0	34.7	7.3	59.3	8/8	10.4	8.0	−15.1	13.1	34.7580	−116.92135	70	10
	lwp5	510	18.5 ± 0.2[e]	37.3	49.1	7.3	85.7	6/6	−3.3	9.6	−0.7	13.1	34.7568	−116.91971	70	10
	lwp6	710	18.5 ± 0.2[e]	37.9	47.8	6.0	85.2	8/8	−2.7	8.1	−2.0	12.7	34.7568	−116.91717	70	10
	lwp7	900	18.5 ± 0.2[e]	29.2	54.1	8.2	67.7	6/6	−11.4	11.7	4.3	13.4	34.7577	−116.91533	70	10
	lwp8	1070	18.5 ± 0.2[e]	37.6	47.9	8.0	57.5	7/7	−3.0	10.2	−1.9	13.3	34.7575	−116.91325	70	10
	lwp9	1210	18.5 ± 0.2[e]	41.8	43.0	9.1	44.7	7/7	1.2	10.6	−6.8	13.8	34.7583	−116.91197	70	10
	lwp10	1430	18.5 ± 0.2[e]	40.6	49.8	5.9	90.3	8/8	Reference Site	Reference Site	Reference Site	Reference Site	34.7585	−116.90984	70	10

[a]Line and plane fits for each sample were calculated following *Kirschvink* [1980]. Site mean directions were calculated following *Fisher* [1953] and tilt correction applied, if any. Rotation and flattening were determined following the methods of *Beck* [1980] and *Demarest* [1983] by using the furthest site from the fault as a reference site. Unit 3 of the Black Mountain basalt was correlated to areas not mapped by *Oskin and Iriondo* [2004].
[b]*Oskin et al.* [2007].
[c]Unit 3 of Black Mountain Basalt is confined between units dated 3.77 ± 0.11 Ma unit 2 and 3.74 ± 0.05 Ma unit 4. Because the older age overlaps the younger including uncertainty, this age is cited for unit 3.
[d]*Oskin and Iriondo* [2004].
[e]*Nielson et al.* [1990].

correction was applied using Paleomag software 3.1 [*Jones*, 2002]. Rotation and flattening were determined following the methods of *Beck* [1980] and *Demarest* [1983] by using the furthest site from the fault as a reference site.

[14] All but two of 23 sites investigated gave rotation values that cannot be distinguished significantly from zero (Table 1, Figure 6). A paleomagnetically reversed declination of $186° ± 5°$ was measured for Site bfd06, sampled from basaltic flow 4 of the Black Mountain basalt field [*Oskin and Iriondo*, 2004] adjacent to the Blackwater fault. All other sites in this area, sampled from basaltic flow 3, gave declinations of 180° to 174° that overlap within error. The slight declination anomaly of basaltic flow 4 may be a result of secular variation of the magnetic field and thus it is not certain whether it reflects actual rotation. *Valentine et al.* [1993] show paleomagnetic declinations in the Black Mountain basalt that are similar to those of site bfd06 and relate these to secular variation. Modest rotation of $10° ± 8°$ was observed for site Lwp 3–4, sampled from the Peach Springs tuff adjacent to the Lenwood fault. This rotation is within error of most of the other sites next to the Lenwood fault as well as with the reference point (Inclination = 33°, Declination = 36.4°, $α95 = 3.4°$) determined by *Wells and Hillhouse* [1989] at the Colorado Plateau.

2.3. Distribution of and Offsets Along Secondary Faults Within OFD Zones

[15] Measurements of secondary fault distribution provide insights into the width, level of activity, mechanism, and distribution of displacement in OFD zones. Mapping of the Pisgah fault zone where it cuts two flows of the Sunshine Peak basalt field shows abundant secondary faulting that extends up to ~400 m from the main fault trace (Figure 7). Secondary faults cutting both flows form scarps up to several meters high and are oriented ~30° relative to the main Pisgah fault. In general, these faults are exposed in uplifted, folded areas (Figure 7). Some of the secondary faults can be followed through the volcanic units into the underlying basement and sedimentary rocks. Tuff deposits overlain by the $752 ± 110$ ka Lavic Lake lava flow [*Oskin et al.*, 2008] are offset by $785 ± 125$ along a well-defined fault trace. Channels incised in the younger adjacent Sunshine peak basalt flow are offset only $130 ± 70$ m.

[16] Next to the Harper Lake fault, secondary fault B, parallel to and 600 to 800 m east of the main fault, offsets multiple lithologic contacts by $179 ± 6$m (fault B in Figure 4 and Figure 8). This fault also offsets an undated alluvial fan deposit by $13 ± 2$ m at 117°01′37.31″W 34°57′24.9″N (Figure 8).

3. Data Analysis

[17] Mylonitic lineations measured adjacent to the Harper Lake fault may be used to quantify the style and amount of distributed deformation accomplished through rotation. First, we show that the variance of mylonitic lineation directions increases toward the fault. Then we use this variability to constrain the maximum sizes of hypothetical fault-bounded blocks that make up the zone of distributed displacement. Using these block dimensions, we estimate the density of secondary faults within the OFD zone. This density is described by a dimensionless number, $ρ_f$, that is

the ratio of secondary fault strike-length per unit distance along the main fault. We also integrate over the rotated blocks to quantify the amount of distributed displacement through rotation.

3.1. Variability of Mylonitic Lineation Directions as Function of Distance Along and From the Fault

[18] To quantify patterns of block rotation next to faults we used simple statistical tools to analyze the variability of the mylonite rotation next to the Harper Lake fault (Figure 9). To trace the existence of trends in the rotation data we use a moving window over 50 measurement points to calculate standard deviation of azimuthal rotation values as well as the $α_{95}$ value of the summed vector [*Fisher*, 1953]. The analysis shows that the variation of mylonite rotation increases nonlinearly toward the fault in both two and three dimensions (Figures 9a, 9b, and 9e) starting at ~400 m from the main fault trace (when the effects of secondary fault B are discarded). The analysis also shows an increase in mylonite rotation variation next to secondary fault B (Figure 5). To the extent that mylonite rotation variation is proportional to the intensity of deformation, the width of the OFD zone (W) next to the Harper Lake fault is ~400 m (excluding secondary fault B). Analysis of stacked mylonite rotation data versus distance from the fault for different fault sections show that along strike the pattern of mylonite rotation varies (Figures 9c and 9d).

3.2. Block Dimensions Within the OFD Zone

[19] We use the azimuthal component of mylonite rotation values to estimate the sizes of fault-bounded blocks that comprise the OFD zone. Due to the pervasively fractured nature of the mylonite adjacent to the Harper Lake fault, major block boundaries cannot be mapped directly. Thus instead we examine the variance of mylonite rotation to define blocks. To estimate the permissible rotation variance within a block we calculate the standard deviation of the differential azimuthal angle in the region > 400 m from the main fault. In this area, the standard deviation of the differential azimuthal angle is approximately constant with distance from the fault (Figure 9e, excluding the effect of secondary fault B) and probably represents an upper boundary for the standard deviation of mylonite orientations within one rigid block next to the Harper Lake fault. We then adopt a value of 2 standard deviations (19.2°) as the permissible variance of the azimuthal component of rotation within small rigid blocks in the OFD zone. We calculate 2-D block dimensions in several steps using a simple computer program to analyze all possible combinations of points that make up blocks. First, a measurement point is chosen and its azimuthal component of rotation compared to its closest neighbors ordered by distance. When a neighboring point is found that has a rotation angle that differs by >19.2°, we interpret its distance as a distance between points located on different blocks. The program then backs up to the previous point compared, which is the furthest of a set of distance-ordered points with rotation values that differ by ≤19.2° from the measurement point. This distance, L, is interpreted as the furthest distance between points located on the same block. Repetition of this process for all measurement points in the data set provides each point with an associated L value. If block
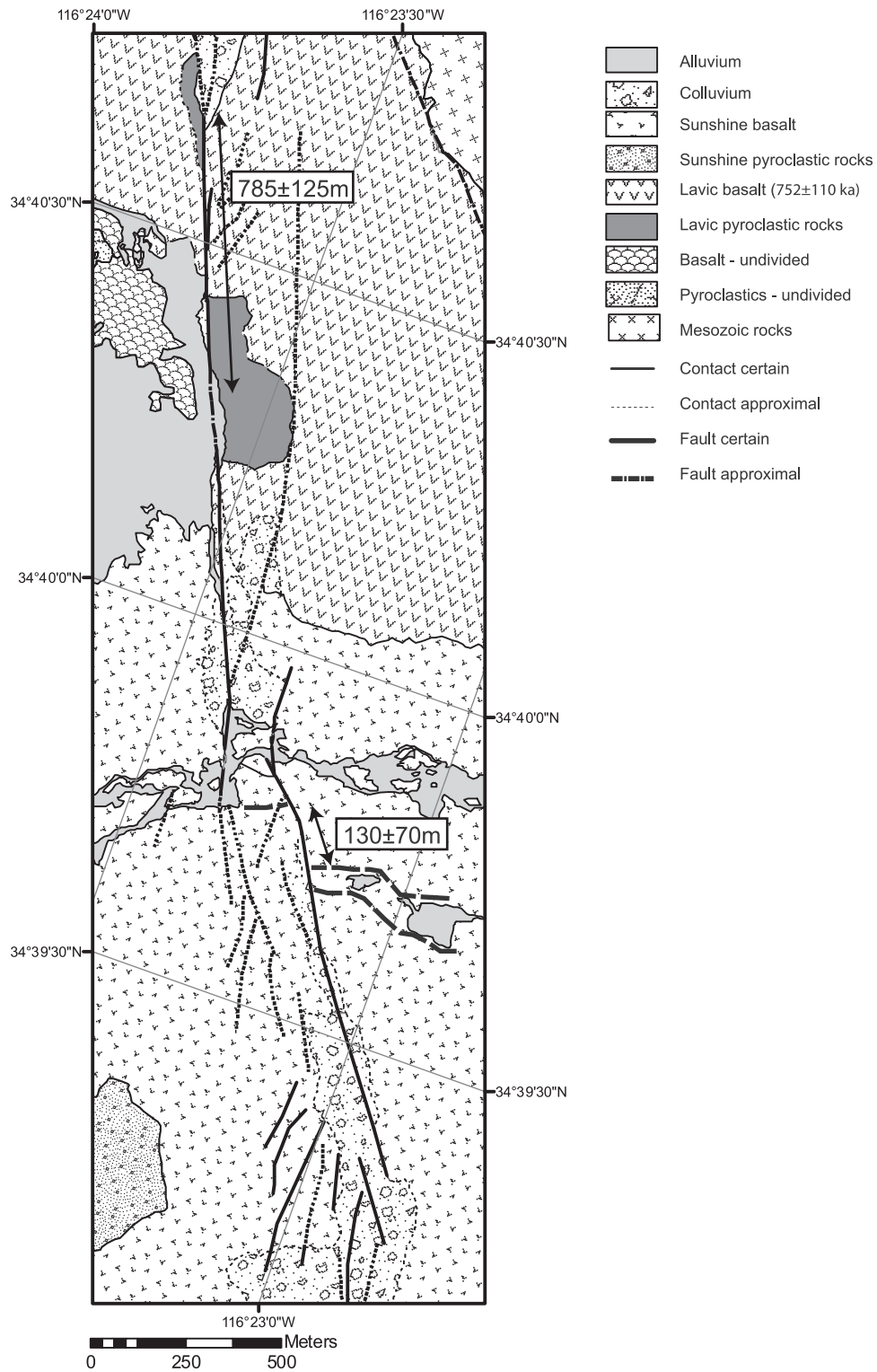
Figure 7. Map of the Pisgah fault where it cuts the Sunshine Peak basalt field on the Twentynine Palms Marine base. Map was produced through air photo interpretation, reinterpretation of earlier studies [*Wilbur*, 1980; *Hart*, 1988], and limited fieldwork. Pyroclastic rocks overlain by the 752 ± 110 ka Lavic Lake basalt flow [*Oskin et al.*, 2008] are offset by 785 ± 125 m along a well-defined fault trace. Channels established across the younger Sunshine peak basalt flow are offset only 130 ± 70 m. Note the concentrations of secondary faults southwest and northeast of the fault. Both of these localities coincide with folding of the basalt flows.
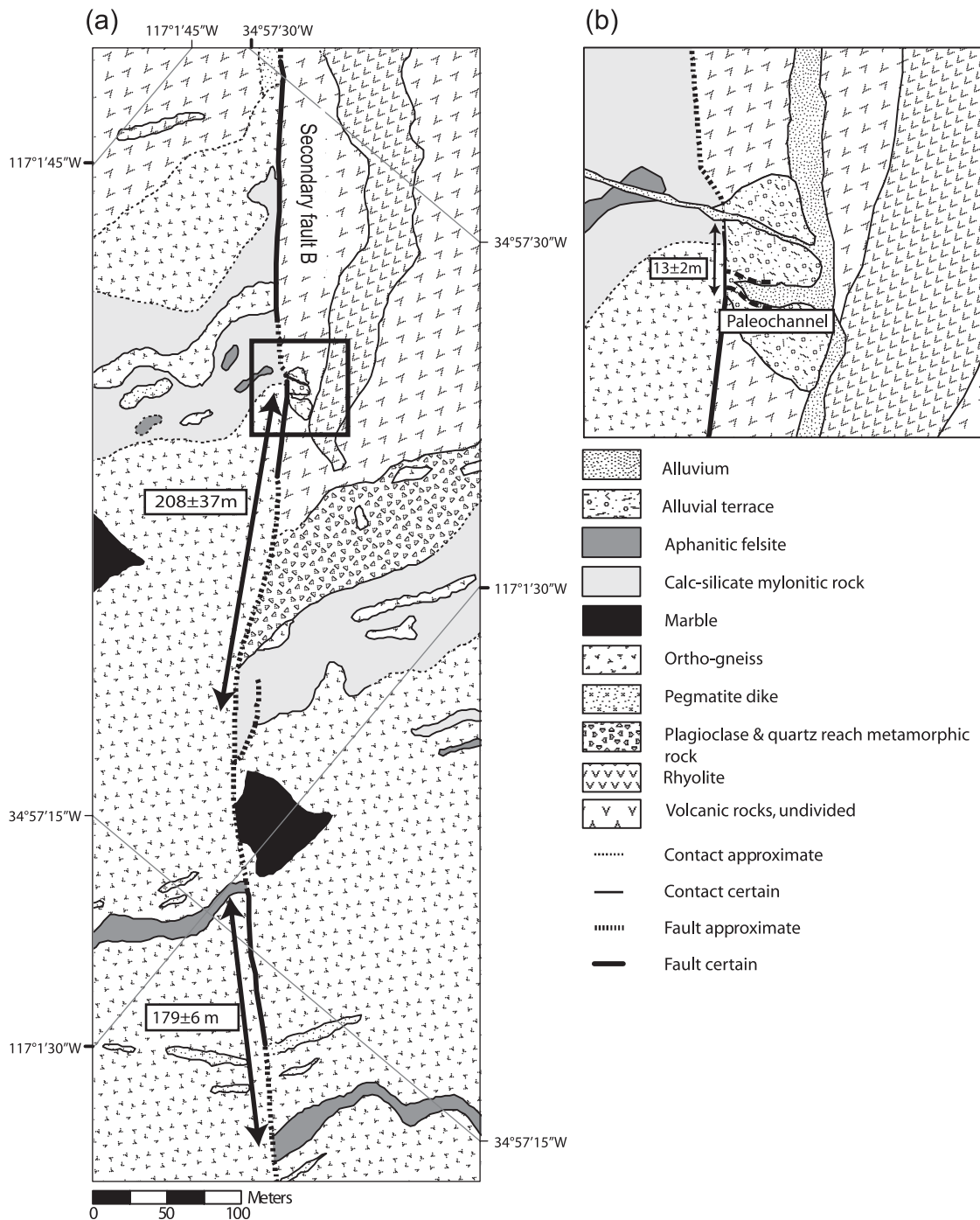
Figure 8. (a) Geologic map of lithologies offset by secondary fault B, located near the Harper Lake fault. Arrows mark offset of pegmatite dike (Pgm) and of calc-silicate mylonitic rock (Csm). Note that the marble (Mb) and rhyolite flow (Ry) units are also offset. (b) Inset map of stream channel incised into an alluvial fan and offset 13 ± 2 m by secondary fault B.

dimensions are much larger than the spacing between measurement points, and if each rigid block is distinguished from the surrounding rigid blocks by rotation angles >19.2°, then L values from a particular block should be largest for measurement points nearest the center of that block. Hence, the largest L value per block (L_{max}), is a gross approximation of the half-length of the shortest axis of a block.

[20] To estimate L_{max}, we have to exclude all L values measured from data points located close to block margins. This is done by excluding all points with L values that are included entirely within larger blocks. Partly overlapping blocks (approximated by circles in Figure 10a) are not excluded because these represent different possible block configurations. We further exclude L_{max} values deter-
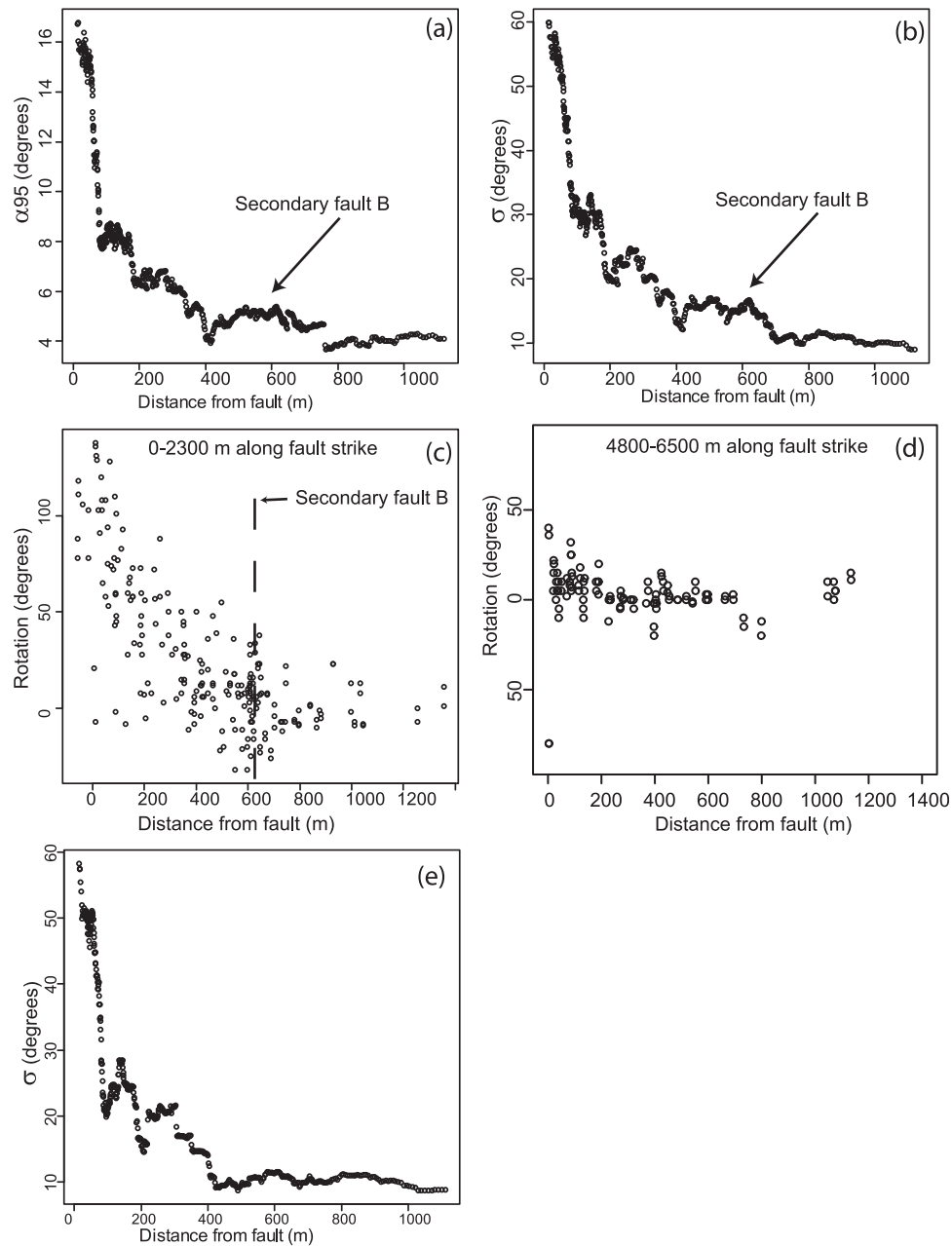
Figure 9. Analysis of distributed rotation of mylonitic lineation adjacent to the Harper Lake fault. (a) α_{95} and (b) standard deviation of azimuthal rotation, presented versus distance from the Harper Lake fault. Values are calculated by a moving window over 50 measurement points. (c and d) Different patterns of the azimuthal component of mylonite rotation along portions of the Harper Lake fault. Figure 9c is the northernmost portion of the area studied, near secondary fault B. Figure 9d is approximately the southern third of the study area shown in Figure 4. (e) Same as Figure 9b, only excluding the data next to secondary fault B.

mined for blocks that include less than five measurement points in order to reduce the effect of erroneous measurements and ensure that the blocks we define are not solely artifacts of the irregular spatial distribution of our measurement points. We also conducted a test of our algorithm with subsets of the mylonite orientation data set. Even when filtered to yield a more regular spatial distribution of measurement points we find that block sizes diminish systematically toward the Harper Lake fault (Figure 11).

[21] Overall, this analysis shows that modeled block dimensions tend to increase away from faults. This is especially clear at the northern section of the Harper Lake fault (Figures 10a and 10b). Here the half-length of the shortest axis of blocks (L_{max}), plotted against the distance (X) between the fault and the locations of these block centers (the measurements at the center of the circles in Figure 10a) shows that the decrease in modeled block dimensions is a simple function of distance from the fault
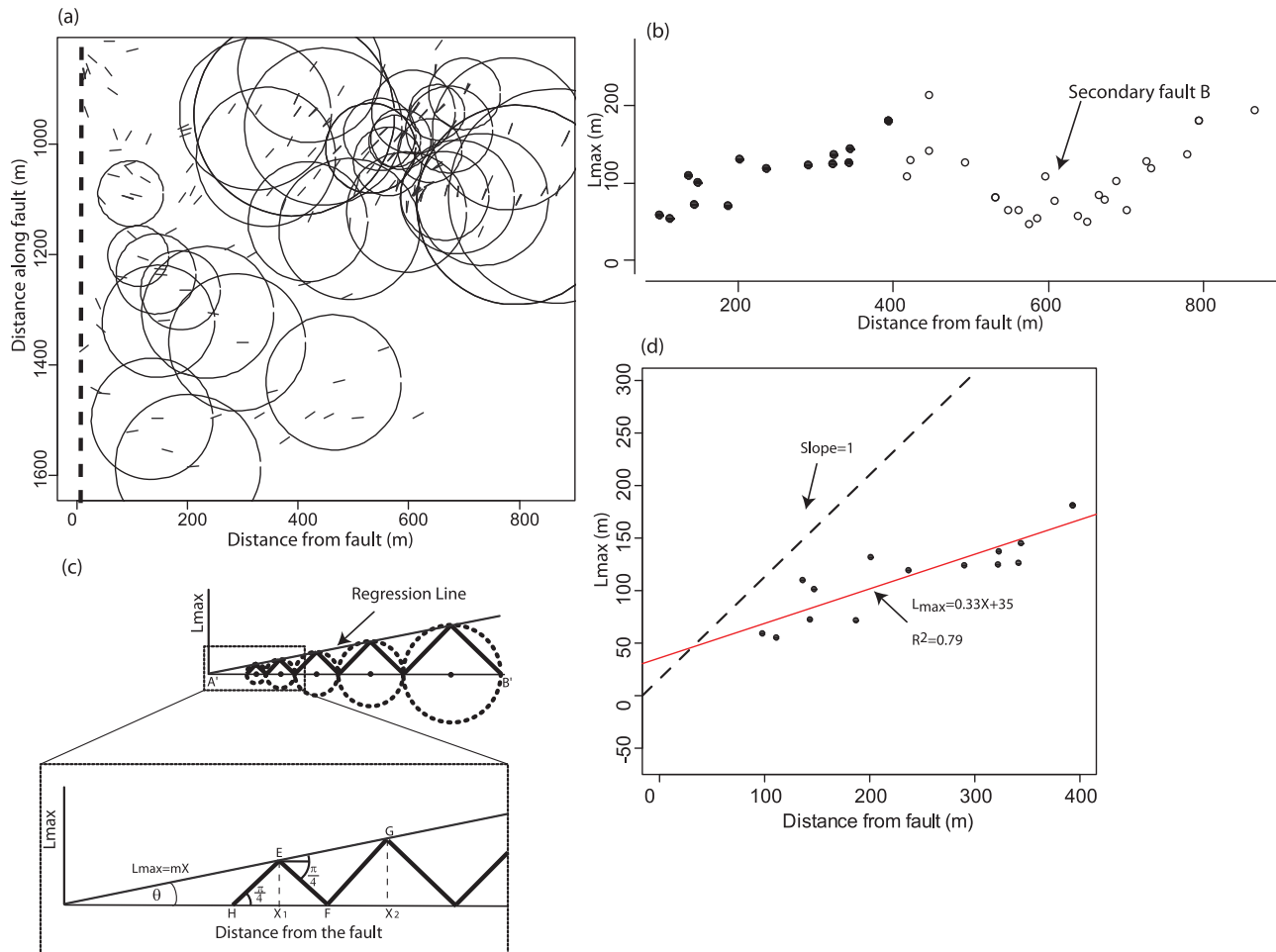
Figure 10. Analysis of block size along the northern portion of the Harper Lake fault. (a) Circles of radius L_{max}, centered at a measurement point (small gray lines) that is interpreted to be near the middle of the shortest axis of a block. Distance along fault is measured southward from the northern edge of the Harper Lake fault in the study area. (b) A plot of modeled L_{max} values versus distance from the fault (X) for all blocks that include ≥ 5 measurement points at this portion of the fault. L_{max} values are plotted versus the distance of the central measurement point from the fault. Note that block dimensions within the 400 m wide OFD zone of the main fault (solid circles) decrease toward the fault. The decline of L_{max} from 400 to 600 m of the fault is attributed to decrease in block size next to secondary fault B. (c) Diagram of the minimal number of circular blocks within the OFD zone idealized by circular blocks of increasing radius posted side by side and bounded by the regression line from Figure 10b. The inset shows geometric relationships used for calculation of the number of large blocks in the OFD zone, n (see Appendix A). (d) The functional relationship between block size and distance from the fault is estimated through a linear regression (solid line) through the data points within 400 m from the fault. The dashed line with 1:1 slope shows the boundary above which blocks would overlap the main fault. The lack of L_{max} above this line supports that this analysis captures the formation of blocks within the OFD zone.

(Figure 10d). Linear regression of L_{max} versus X to estimate this function for the 400 m wide OFD zone yields

$$L_{max} = 0.33X + 35 \qquad (1)$$

with $R^2 = 0.79$ and slope error $= 0.05$ (Figures 10b and 10d). We associate the decrease and increase of L_{max} values at 400–1000 m from the fault (Figure 10b) with secondary fault B (Figure 5).

[22] Theoretically, L values larger than X, the distance from the fault, should not occur because the main fault must define a block boundary. For the same reason the L_{max} value at distance zero from the main fault should be zero. The fact that none of the L_{max} values in the analysis is larger then the distance from the main fault, as well as the low intercept value of block axis length (35 ± 13 m) supports the validity of our approach.

3.3. Secondary Fault Density Within the OFD Zone

[23] The ratio between the length of secondary faults and the main fault, if secondary faults are active during seismic events, is important in order to understand the role of OFD
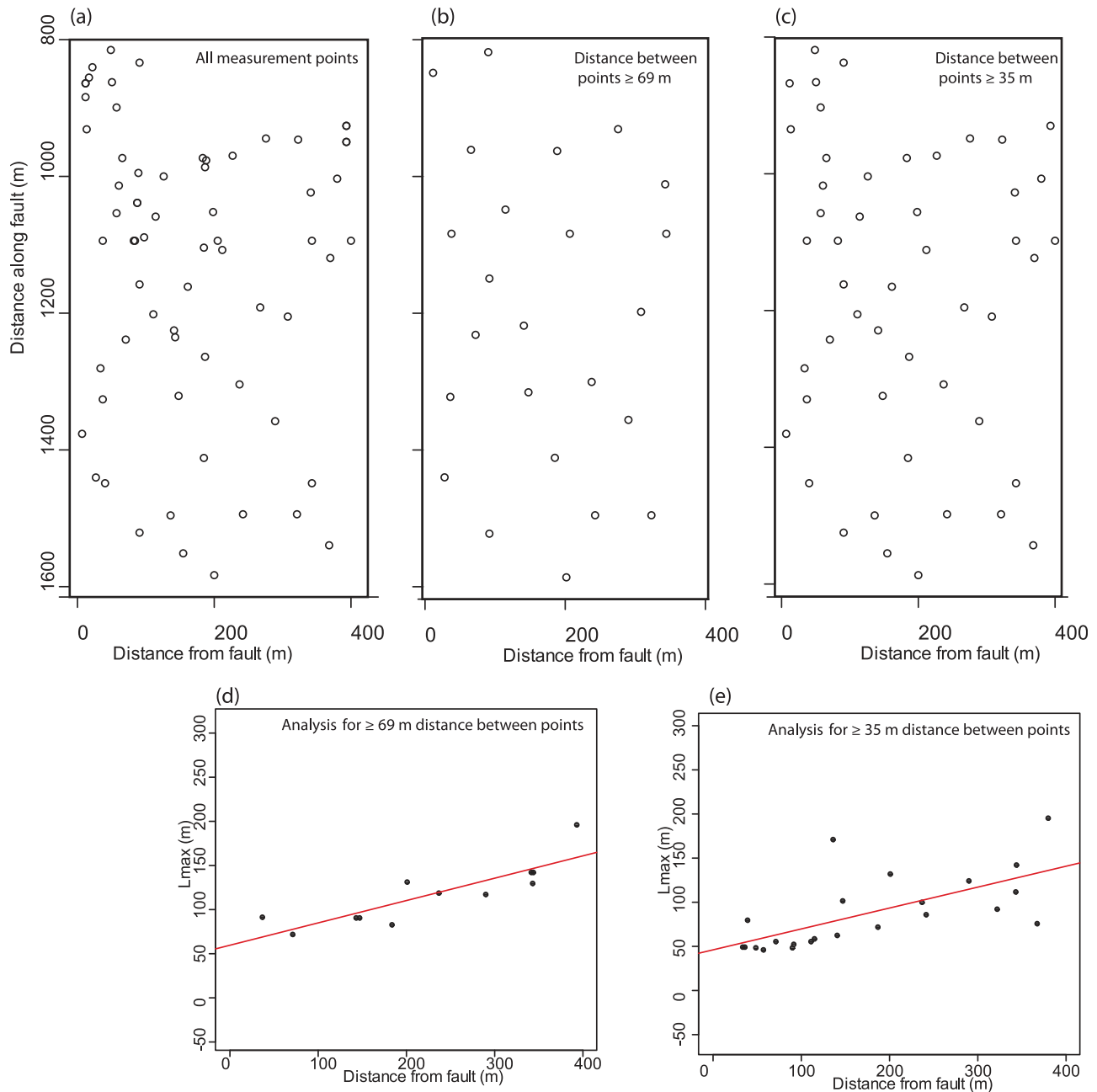
Figure 11. Effects of data spacing on block size analysis. (a) Distribution of mylonitic lineation measurements in the northern fault section within 400 m from the fault, all measurements included. (b and c) Examples of randomly generated instances of semiregular data spacing based on a minimum distances of 69 m and 35 m between measurement points. These minimum distance values represent the mean and half mean distances between measurement points in the analysis area. Multiple, semiregular measurement sets were generated by randomly ordering the original data set and applying an order-based filter that removed points closer than a specified minimum distance from each other. (d and e) Examples of block size analysis for the two data-spacing instances shown in Figures 11b and 11c. Here we restrict blocks to include two or more data points (instead of five or more in the original analysis) because the proximity filter already excludes the majority of adjacent measurement points. For a minimum distance of 69 m, 98% of all random, semiregularly spaced data sets (n = 1000) generated a positive slope (mean slope = 0.18 ± 0.11), indicating that block size diminishes toward the fault. For a minimum distance of 35 m, all random data sets generate a positive slope (mean slope = 0.28 ± 0.04). The consistent return of positive slope values demonstrates that the trend of diminishing block sizes toward the fault is not an artifact of uneven data distribution.

as a sink of seismic energy. We estimate this ratio (i.e., the secondary fault density, ρ_f) by calculating the cumulative circumference of modeled blocks bounded between the main fault and the outer margins of the OFD zone. For this analysis we assume that the modeled blocks are equidimensional and can be modeled as circular blocks with a radius of L_{max}. Because L_{max} is an estimate of the half-length of the short axis of blocks, this approach will overestimate the density of secondary faults if blocks are elongate. However, we also neglect smaller blocks that are certain to lie between larger ones, as well as subhorizontal faults that may bound some blocks. Thus, overall the estimate of secondary fault density is conservative. The change of block size versus distance from the fault modeled in section 3.2 is used to calculate the minimum number of blocks within the OFD zone. Then, we use the cumulative circumference of these modeled blocks, per unit distance along the main fault as a measure of secondary fault density.

[24] In order to calculate the cumulative circumference of blocks within the OFD zone we find the number of modeled blocks that fit into the width of the OFD zone (W), where block radius, L_{max}, increases as a function of X (Figure 10b). The minimal number of blocks (n) within the OFD zone occurs when modeled blocks are arranged side by side as shown in Figure 10c. The geometric relationships presented in Figure 10c are used to derive an equation for the number of blocks within the OFD zone (Appendix A),

$$n = \frac{\log(X_n/X_1)}{\log[(1+m)/(1-m)]} + 1, \qquad (2)$$

where m is the slope of the regression line that expresses L_{max} as function of distance from the fault. X_n is the distance from the fault of the center of the farthest block from the fault, and X_1 is the distance from the fault of the center of the closest block to the fault. It is important to note that X_1 must be a finite minimum distance, otherwise n is infinite. In order to get a conservative estimate of n, we calculated X_1 assuming that rigid blocks start at the edge of the fault gauge zone, about 1m from the fault at a maximum [Chester et al., 2005]. Thus, n represents the number of blocks bounded between 1 m from the fault to the outer edge of the OFD zone at distance W from the fault.

[25] For 400 m wide OFD zone we used an m (slope) value of 0.33 ± 0.05 derived from the regression Lmax versus distance from the fault in (1). For this m value, we calculate that the number of modeled blocks within the OFD zone (n), as ~9. By calculating n we can then calculate secondary fault density as the ratio, ρ_f, between the summed lengths of modeled secondary faults within OFD zone to the length of the adjacent main fault. To do this we calculate the number of blocks of different radii that can fit into a swath defined by the diameter of the largest block and the main fault. Appendix A shows that $\rho_f = n\pi$. This suggests that the length ratio of modeled secondary faults to the main fault is ~27 ± 4. This ratio may overestimate ρ_f because actual blocks may share the same bounding fault. However, smaller blocks probably fill the gaps between larger, equidimensional blocks and this would increase ρ_f. Hence, this is a likely a reasonable lower bound on the ratio of secondary fault length to the length of the master fault.

3.4. Rotational Shear Displacement Accommodated Within the OFD Zone

[26] The magnitude of rotational displacement and its fraction of the total displacement may shed light on the uncertainty involved with slip estimates based solely on offset along faults. The minimum rotational shear displacement occurs in the southern portion of the Harper Lake fault study area where there is no significant mylonite rotation (Figure 9d) and is thus approximately zero. The maximum rotational shear displacement occurs in the northern portion of the study area where a continuous change in the azimuthal component of mylonite rotation is observed within the OFD zone (Figure 12a). In this area, systematic rotation occurs only with respect to the vertical axis. Therefore, the displacement calculations based on the azimuthal component of mylonite rotation encompass the major component of rotational displacement.

[27] Rotational shear displacement is calculated by integration of the azimuthal component of rotation over the width of the OFD zone (W). At the northern section of the fault, W is estimated as ~485 m by finding the cutoff distance that divides the data set into two groups with the greatest difference of mean mylonite rotation. This estimate of W is greater than the earlier estimate of 400 m because it also accounts for rotation adjacent to secondary fault B. For the subset of data between the fault and W, we fit a linear regression to estimate the relationship between the azimuthal component of mylonite rotation (θ) and the distance from the fault (Figure 12a). For the northern section of the data set, starting next to secondary fault B, the regression yields $\theta = 1.3–0.0025x$, $R^2 = 0.4$, where θ is in radians and x is distance from the fault in meters. The continuous change of the azimuthal component of mylonite rotation within the OFD zone in this area, starting next to secondary fault B, suggests that rigid block dimensions are much smaller than the width of deformation zone. This could justify the use of a continuum model to calculate the shear displacement [Lamb, 1987, Kimurah et al., 2004]. The continuum model is analogous to elongate blocks that change shape with rotation (Figure 12b). From such a model the calculated shear displacement is

$$D = \int_0^w \tan[\theta(x)]\, dx = \int_0^w \tan(mx) dx \qquad (3)$$

after Kimurah et al. [2004]. This results in rotational shear displacement, D, of 600 ± 100 m. Using this model, however, requires internal deformation of blocks as rotation proceeds (Figure 12b). Circular blocks, on the other hand, can rotate in a ball bearing fashion [Beck, 1976; Greenhaus and Cox, 1979; Brown and Golombek, 1985; Schouten et al., 1993], without requiring internal deformation of blocks. Therefore, it is a simpler model for areas where significant block rotation is observed. For circular blocks,

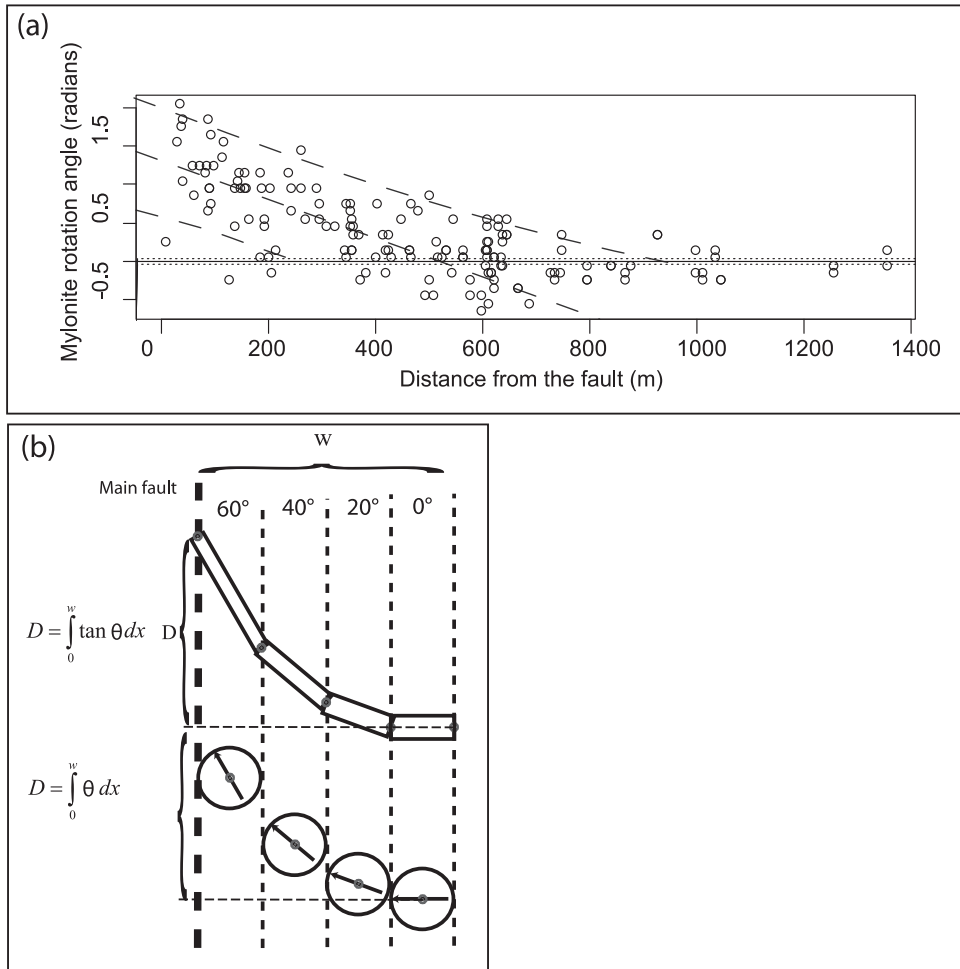$$D = \int_0^w \theta(x) dx = \int_0^w mx dx. \qquad (4)$$

Figure 12. Magnitude of distributed displacement via rotation. (a) Azimuthal component of mylonite rotation data at the northern section of the Harper Lake fault. Rotation is calculated with respect to the mean far field azimuth of 224°. Negative rotation values represent counterclockwise rotation. Solid line shows a linear regression of rotation versus distance from the fault. Dashed lines mark the 95% confidence belt for the regression mean (−0.0025 ± 0.0003). Horizontal solid and dashed lines mark the mean mylonite and the associated standard error of the mean for the mylonites rotation outside of the OFD zone (0 ± 0.03 radians). The intersection of these regression lines determines the bounds of integration used for displacement calculation. (b) Conceptual illustration of two different models for calculation of shear displacement due to a linear increase in rotation angle toward a fault. The two models produce different estimates of displacement. The width of the OFD zone is a constant, W, in these models, as is the amount of rotation at a given distance from the fault. Bold black lines mark block boundaries and gray dots mark rotation axes. Bold dashed lines mark major block bounding faults. Rectangular blocks idealize the continuum model of rotation. Note that the rectangular blocks must deform internally in order to maintain their area. Such area problems may cause strain in the third dimension, out of the figure plane. Rotation values approaching 90° yield infinite, unrealistic, displacement values for elongate blocks. Circular blocks, on the other hand, rotate without internal deformation and yield realistic displacement values for high rotation angles. Thus, the integrated displacement for circular blocks is lower than for elongate blocks. Note that the vertical distance between the centers of adjacent circular blocks equal to two times the arc length defined by the block radius times the angle of rotation.

This results in D of only 360 ± 60 m. The difference in D calculated with these different methods is a result of the elongation of blocks that is implied by integrating over the tangent function. This results in a nonlinear increase of D with rotation angle (Figure 12b). Error is incorporated into estimates of D (Figure 12a) by Monte Carlo simulation of 1000 repetitions sampling from the distribution of far field mean rotation angle (0 ± 0.03 radians and from the distribution of regression slopes deduced from the OFD zone data set (−0.0025 ± 0.0003).

[28] It is important to note that the distributed displacement calculated here is only on one side of the Harper Lake fault. If distributed displacement is symmetric across faults (see section 4), then these displacement values, measured

northeast of the Harper Lake fault, are only half of the total distributed displacement. The amount of rotational shear displacement is comparable to the amount of offset on secondary fault B (Figure 8). This indicates that distributed rotational shear displacement accounts for significant portion of the total displacement adjacent to the Harper Lake fault.

4. Discussion

[29] In this section, we synthesize observations from the Mojave Desert region to develop an understanding of OFD zones and their significance. First, we review the assumptions underlying our interpretation of distributed displacement. Then, we discuss the characteristics of OFD zones, including the magnitude of distributed displacement, the width of the zones, and the distribution of displacement within these zones. Last, we discuss structural aspects of the OFD zone – its level of activity, the structural mechanisms of strain accommodation, and the possible interactions between damage-induced reduction of shear rigidity and observed distributed displacement.

[30] The assumption of original linearity of OFD markers is fundamental to the displacement and block size calculations. This assumption is supported by the clear association of deflected mylonitic lineation directions with the Harper Lake fault (Figure 4) and the deflection of the Silver Bell fault within 500 m from the Calico fault (Figure 3) [*Oskin et al.*, 2007]. At a smaller scale, a secondary fault next to the Harper Lake fault (fault A in Figure 4) also shows deflected mylonitic lineation directions associated with it (Figure 5). Though deflection could arise for features emplaced next to existing faults due to the distorted stress field next to the fault [*Zoback et al.*, 1987], this is not the case for the mylonitic lineation and the Silver Bell fault because these markers predate initiation of faulting along the Harper Lake and Calico faults [*Bartley et al.*, 1990; *Glazner et al.*, 2000].

[31] To evaluate the contribution of distributed displacement to total displacement across fault zones we assume that distributed displacement is symmetric across faults. The example of symmetric deformation surrounding secondary fault A next to the Harper Lake fault (Figures 4 and 5) and the symmetry of deflection of the Silver Bell fault (Figure 3) [*Oskin et al.*, 2007] across the Calico fault both support this assumption.

[32] In the analysis of mylonitic lineation directions, we assumed that the rotation angle is the smallest angle between lineation directions. It is important to note that unlike paleomagnetic measurements, most of our measurements of mylonitic lineation provided only orientation. In a few key areas we also measured kinematic shear sense indicators in order to constrain rotations greater than 90° (Figure 4). Other measurements without shear-sense indicators that show an apparent counterclockwise rotation are probably also due to clockwise rotation >90°.

[33] The assumption of equidimensional blocks approximated geometrically as circles is fundamental to the calculation of the length ratio between secondary faults and the main fault. Circular blocks were used in the past to model areas of high block rotation [*Beck*, 1976; *Greenhaus and Cox*, 1979; *Brown and Golombek*, 1985; *Schouten et al.*, 1993], they minimize volume problems and internal defor-

mation caused by rotation of elongate blocks and allow for high rotation values without yielding unrealistically large displacement values (Figure 12).

4.1. Magnitude of Distributed Displacement

[34] Of all faults in this study OFD magnitude was quantified only next to the Harper lake and Calico faults (Table 2). To generalize our observations to other faults, the magnitude of distributed displacement for the Harper Lake fault and Calico fault is scaled by the total displacement across each fault. Total displacement is estimated from markers projected to each fault from outside of the OFD zone. For the Calico fault, 2.2 km of distributed displacement divided by 9.8 km of total displacement [*Oskin et al.*, 2007], results in 23% of displacement via OFD. For the Harper Lake fault, the maximal distributed displacement is estimated by summing the components of vertical axis rotation and secondary fault slip in a portion of the study area. Here, 179 ± 6 m of displacement occurs across a secondary fault (fault B in Figure 4), and either 360 ± 60 m or 600 ± 100 m of displacement via distributed vertical axis rotation. Summing the rotational and fault slip components, and multiplying it by 2 due to symmetry across the fault, results in 1080 ± 130 or 1600 ± 200 m of distributed displacement, depending on the model of block rotation used. This sum is a lower bound due to possible unrecognized displacement along other secondary faults. Dividing the calculated distributed displacement values by 3500 ± 500 m of total displacement across the Harper lake fault [*Bartley et al.*, 1992; J. Fletcher, personal communication, 2004], results in relative magnitudes of $31 \pm 4\%$ and $46 \pm 6\%$. These results, in agreement with previous studies [*Nelson and Jones*, 1987; *Miller and Yount*, 2002; *Kimurah et al.*, 2004] strongly suggest that displacement estimates that do not account for distributed displacement may be significantly underestimated. Such estimates are prone to occur when displacement estimates along strike slip faults are based on channel offsets with narrow aperture of piercing points [e.g., *Sieh and Jahns*, 1984; *Liu et al.*, 2004; *Fu et al.*, 2005; *Van der Woerd et al.*, 1998]. The analysis of OFD adjacent to the Harper Lake fault showed that rotational shear displacement can account for a significant portion of the total distributed displacement next to faults. Because it is in general difficult to identify this rotational component, especially when mapping offset stream channels, fault displacement rates may be underestimated even in cases where displacement along secondary faults is observed and quantified.

[35] Alternating patterns of mylonite rotation along the Harper Lake fault (Figures 9c and 9d) suggests that the magnitude of distributed displacement via rotation changes along fault strike. These variations appear to support along strike variation in the overall magnitude of distributed displacement. Such changes may be due to along-fault stress variation due to local changes in fault orientation. Alternatively, along strike changes in magnitude of distributed displacement via rotation may be due to trade-off between block rotation and offset along subparallel secondary faults.

4.2. OFD Zone Width

[36] Most of our observations show that distributed deformation commonly occurs within 1 km from major faults in the Mojave desert (Figures 3, 4, 6, and 9) but may extend to

Table 2. Summarized Observation of Distributed Displacement

Fault Section	Distributed Displacement Through Block Rotation	Distributed Displacement by Shear Along Secondary Faults	Magnitude of Distributed Displacement
Harper Lake north	Magnitude is about 20% of total displacement. May be greater if blocks are treated as continuous at their end points.	Displacement is quantified along secondary fault B, Magnitude is about 10% of total displacement on Harper Lake fault. Other, unmapped secondary faults may exist.	Distributed displacement is at least 30% of total displacement across the Harper Lake fault.
Harper Lake south	Not significant.	Displacement along unmapped secondary faults possible.	Unknown, and may not be present.
Harper Lake secondary fault A	Distributed displacement is observed, proportion cannot be quantified because of undetermined offset along secondary fault A.	Displacement along unmapped secondary faults possible.	Present but not quantified.
Harper Lake secondary fault B	Distributed displacement is observed, but not quantified due to high scatter of rotation data.	Displacement along unmapped secondary faults possible.	Present but not quantified.
Calico south (dikes, Silver Bell fault)	Distributed displacement is observed but not quantified separately from shear along secondary faults.	Secondary faulting exists but not quantified separately from rotational displacement.	Distributed displacement is ~20% of total displacement across the Calico fault.
Calico north (Pipkin basalt flow)	Not significant since basalt emplacement ca. 740 ka [*Oskin et al.*, 2007].	Displacement along unmapped secondary faults possible.	Unknown, and may not present.
Lenwood at Stoddard Valley	Not significant.	Secondary faulting is observed [*Strane*, 2007].	Present but not quantified.
Blackwater at Black Mountain	Not significant since basalt emplacement ca. 3.6 Ma [*Oskin and Iriondo*, 2004].	Secondary faulting observed, not quantified.	Present but not quantified.
Blackwater at Black Hills	Not significant.	Secondary faulting observed, not quantified.	Present but not quantified.
Pisgah at Sunshine Peak	Unknown.	Secondary faulting observed, not quantified.	Present but not quantified.

~1.5–2 km from the fault (Figure 4d). The outer boundary of the OFD zone may vary and is often not well defined because of a gradual decrease in the amount of deformation. The width of the OFD zone may also change along fault strike (Figure 9c and 9d). Secondary faults next to the Harper lake fault have their own, narrower (20–30 m), OFD zones (Figure 5).

[37] Similar widths of the OFD zone were found in studies of surface deformation from the Landers and Hector Mine earthquakes. These studies show that inelastic deformation often occurs within 50–200 m from the main fault trace, and may extend for up to 1700 m from the main fault trace [*Johnson et al.*, 1994; *McGill and Rubin*, 1999; *Treiman et al.*, 2002; *Michel and Avouac*, 2006]. The width of the OFD zone during a single earthquake may depend on stress conditions (and thus on fault orientation), rupture velocity, and rock strength and may change due to structural complexity of the fault trace [*Johnson et al.*, 1994; *Rice et al.*, 2005].

4.3. Distribution of Shear Displacement Within the OFD Zone

[38] Overall, observations from the Mojave Desert suggest that distributed displacement increases nonlinearly with distance toward the main fault (Figures 3, 4, and 9). In section 3.2, we fit a linear function to the azimuthal component of mylonite rotation next to the northern portion of the Harper lake study area. Integration of this yields a squared dependence of displacement on distance. An exponential function represents displacement approaching faults almost as well. The intensity of OFD, as represented by the variability of mylonite rotation, also increases non-

linearly toward faults (Figure 9). Studies by *Kimurah et al.* [2004] and *Katz et al.* [2003], using paleomagnetic and structural data, also report a pattern of nonlinear increase in vertical axis rotation toward strike slip faults in Japan and Israel. Taken together, these observations suggest that the nonlinear distribution of displacement within OFD zones is a general pattern that is not unique to the Mojave Desert or to the scale of faults studied.

[39] The nonlinear or exponential displacement pattern is also reflected in coseismic patterns of OFD. Studies of coseismic surface deformation, in the Mojave Desert [*Treiman et al.*, 2002; *Michel and Avouac*, 2006] and elsewhere [*Lawson*, 1908; *Rockwell et al.*, 2002; *Haeussler et al.*, 2004], show a nonlinear decrease in faulting, fracturing, and displacement with distance from the main fault.

4.4. Activity of OFD

[40] OFD may form through accumulation of strain in the damage zone adjacent to thru-going faults or due to accumulation of strain during fault propagation, prior to the formation of a thru-going seismogenic fault [*Passchier*, 2001]. Although we cannot exclude the second option, several observations indicate progressive accumulation of OFD next to active, thru-going faults. First, coseismic surface deformation in the Mojave Desert [*Johnson et al.*, 1994; *McGill and Rubin*, 1999; *Treiman et al.*, 2002; *Michel and Avouac*, 2006] and elsewhere [*Lawson*, 1908; *Rockwell et al.*, 2002; *Rymer et al.*, 2002] shows a wide zone of inelastic deformation, including small-scale block rotation and secondary faulting. A few of these studies quantify the amount of distributed shear displacement [*Lawson*, 1908; *Rockwell et al.*, 2002]. Second, in a few

cases we observe distributed displacement of markers that postdate fault inception (Figures 7 and 8). The Pisgah fault shows a wide zone of secondary faulting in the younger Sunshine Peak lava flow. This faulting post dates at least 600 m of displacement along a well defined fault that displaces the older, adjacent, Lavic Lake lava flow. Thus, activity on these secondary faults coexisted with slip on a well-defined, active, master fault. Next to the Harper Lake fault, a secondary fault with 179 ± 6 m of slip (fault B in Figure 4), cuts young alluvial deposits. *Strane* [2007] also showed secondary faults cutting Quaternary deposits up to 2 km away from the Lenwood fault.

[41] The activity of OFD zones may be important for maintaining zones of reduced rigidity, known as compliant zones, around active faults. The eastern Mojave Desert contains several strike-slip faults with significant dextral slip that have not been active in the Late Quaternary [*Howard and Miller*, 1992]. When *Fialko et al.* [2002] analyzed post-Hector Mine deformation of km-scale compliant zones next to major faults in the Mojave Desert, they did not find compliant zones next to these inactive faults, such as the Bristol Fault, Granite Mountains Fault, or the Broadwell Lake fault [*Dokka and Travis*, 1990; *Glazner et al.*, 2000]. This suggests that wide compliant zones are maintained by active faulting. Healing processes appear to cause compliant zones to regain rigidity once faults cease to be active.

4.5. Structural Mechanism of Strain Accommodation Within OFD Zones

[42] A conceptual model for structure of distributed displacement in OFD zones is presented in Figure 13. Accommodation of distributed displacement occurs by a combination of block rotation and displacement along secondary faults subparallel to the main fault. The proportion between these two displacement components may vary considerably along fault strike. The density of faults, as well as the amount of rotation, increases toward the main fault. This leads to a decrease in block dimensions, and very likely an increase in aggregate secondary fault slip toward the main fault. In areas of significant rotation, blocks are hypothesized to be equidimensional.

[43] The lack of significant rotation from the paleomagnetic measurements provides interesting insights into the relations between block rotation and folding. Except for the one potentially rotated site, bfd06, sites with folding adjacent to the main fault were avoided for paleomagnetic sampling. Conversely, the study areas along the Calico and Harper Lake faults, where significant rotational OFD occurs, are located within zones of modest transpressional folding. Folding and rotation may be associated due to the volume problem caused by rotation of noncircular blocks. Alternatively, higher normal stresses in areas of folding may favor rotation over simple shear along secondary faults.

[44] Where measurable, integrated strain in OFD zones is dominated by normal drag, or drag that contributes shear displacement in the same sense as fault slip. For the dextral faults studied here, normal drag is expressed as clockwise rotation of deflected markers. Though less significant, reverse drag [*Reches and Eidelman*, 1995] may also be present. For example, some mylonite rotation was found to be counterclockwise (Figures 4 and 5). This rota-

tion may be associated with steep local slip gradient along fault strike, local interactions between rotated blocks, or rotation next to antithetic secondary faults. Alternating modes of normal and reverse drag along fault strike are also reported in studies of coseismic distributed displacement next to strike slip faults [*Lawson*, 1908; *Rockwell et al.*, 2002].

4.6. Damage and Displacement Interactions Within OFD Zones

[45] Multidisciplinary observations show correlation between fault compliant zones and the distribution of displacement within OFD zones. The width of distributed displacement zones (up to 1 to 2 km half width, or 2 to 4 km total) is similar to the width of compliant fault zones imaged in the Mojave Desert with InSAR (1–2 km) [*Fialko et al.*, 2002; *Fialko*, 2004]. These widths are also similar to the 1.5 km zone of reduced seismic velocity documented along the Calico fault by *Cochran et al.* [2009].

[46] OFD zones are characterized by a core of more intense deformation [e.g., *Rockwell and Ben Zion*, 2007; *Faulkner et al.*, 2006]. For example, 100–200 m wide zones of intense distributed displacement are observed next to both the Calico and Harper Lake faults (Figures 4, 3, and 9). Studies of coseismic surface deformation also document a 100–400 m zone of more intense distributed deformation [*Johnson et al.*, 1994; *Michel and Avouac*, 2006; *McGill and Rubin*, 1999; *Treiman et al.*, 2002]. The nonlinear increase in distributed deformation toward the fault is further corroborated by seismic velocity studies showing a low-velocity zone of 75–250 m width along faults [*Li et al.*, 1998, 2003; *Li and Vidale*, 2001]. This narrow zone may represent a highly damaged zone next to the fault that is maintained by passing coseismic ruptures [*Cochran et al.*, 2009]. Several studies [*Wilson et al.*, 2005; *Chester et al.*, 2005; *Rockwell and Ben Zion*, 2007; *Dor et al.*, 2006] have focused on the formation of such intensively damaged zones adjacent to faults due to distributed fracturing during passage of a rupture. This fracturing is posited to occur due to large normal stresses imparted by the passing slip pulse, and in the absence of shear [e.g., *Wilson et al.*, 2005; *Brune*, 2001]. While our findings do not contradict the proposed mechanism of such fracturing, we show that significant shear also occurs in the damage zone. It is probable, based on the range of observations presented here, that distributed shear deformation occurs during earthquake ruptures and is not a relic of the early stages of fault formation. This shear is most intense within a narrow, ~100 m wide zone of intense deformation but extends outward beyond this zone by up to a kilometer or more where deformation gradually diminishes to a background level.

[47] The good empirical agreement between the width of compliant zones imaged geophysically [*Fialko et al.*, 2002; *Cochran et al.*, 2009] and the distributed displacement measured from geology suggests the existence of a mechanism that links the two. Such a mechanism could include occurrence of damage during coseismic dynamic rupture propagation along secondary faults that accommodate displacement within the OFD zone. Additional damage may occur by fracturing of rotated block margins due to elevated stress during rotation. Though this damage is permanent
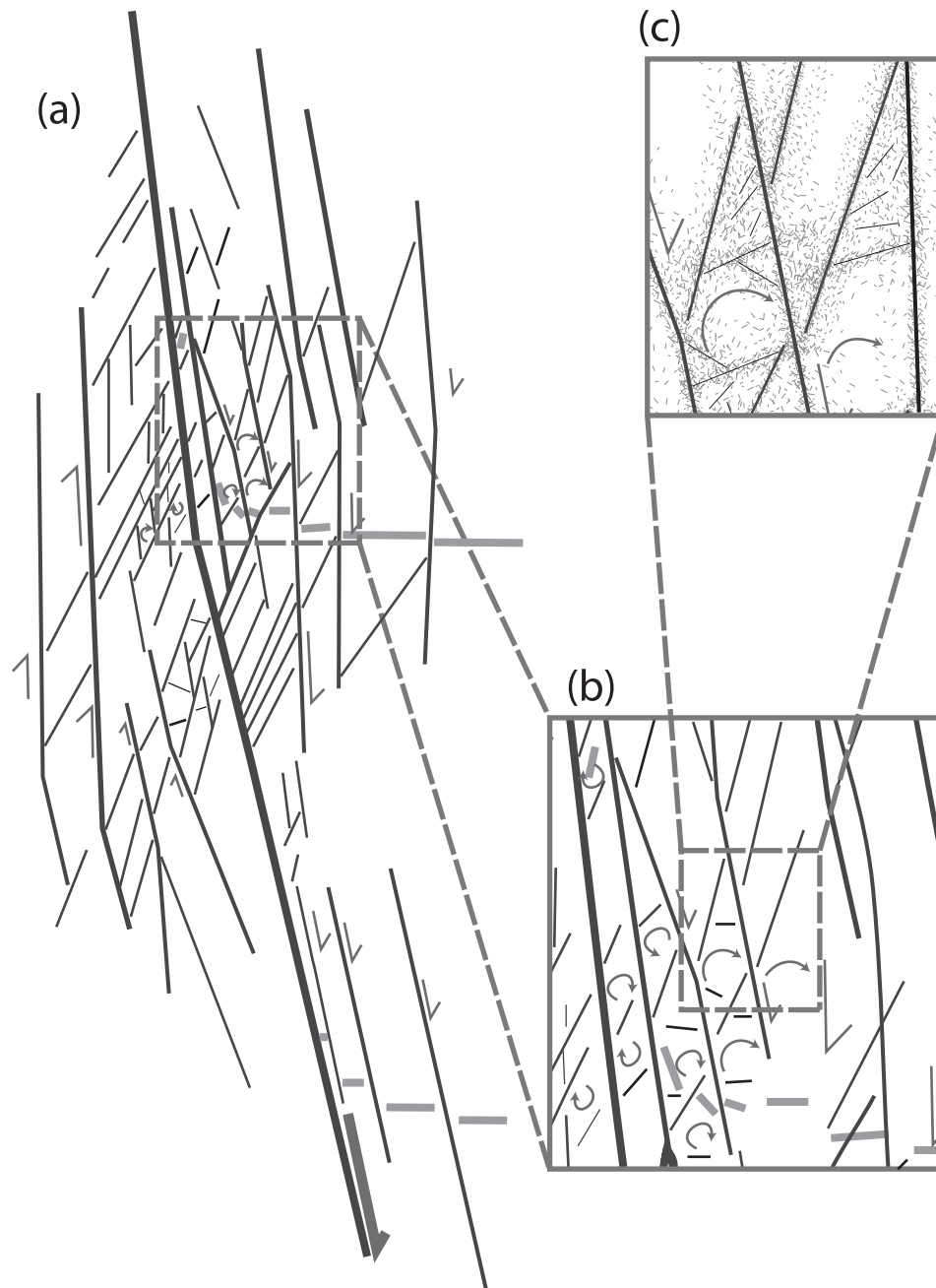
Figure 13. Conceptual model for the mechanisms of distributed displacement. Map view of conceptual model for the mechanisms of distributed displacement in OFD zones. Black solid lines represent faults, gray solid lines represent planar markers, and thin short gray line segments represent damage accrued during fault ruptures (only in Figure 12c). (a) Distributed displacement is accommodated through combination of block rotation and displacement along secondary faults subparallel to the main fault. The proportion between these two displacement components, as well as the magnitude of displacement may vary considerably along fault strike. This variability is illustrated by the differences in how planar markers are deformed as these approach the main fault. The density of faults, as well as the amount of rotation, where present, increase toward the main fault. (b) The dimensions of blocks decrease toward the fault and in areas of significant rotation blocks are probably equidimensional (also illustrated in Figure 13c). Note that some of the blocks may rotate CCW. (c) Damage is probably distributed throughout the OFD zone via the network of secondary faults.

deformation, shear rigidity can recover from damage through a healing process, where cracks within a rock mass gradually relax and close. Healing has been observed on active faults within a span of several years following an earthquake rupture [*Li et al.*, 1998, 2002, 2003; *Li and Vidale*, 2001]. Because of healing effects, distributed displacement is not a direct proxy for the reduction of shear rigidity in fault zones. However, to the extent that damage is proportional to distributed shear displacement, such displacement provides useful insight into the time-integrated pattern of fracture production and the expected distribution of rigidity surrounding active faults.

5. Conclusions

[48] We show that OFD zones adjacent to 30–60 km long, active strike slip faults of <10 km displacement in the central Mojave Desert may account for a significant portion of the total shear displacement. Conservative estimates show that the magnitude of distributed displacement accounts for 0 to ~25% of the total displacement across fault zones. This occurs over zones that are typically 1 to 2 km across, but may in some cases be up to 4 km wide. We find that both displacement magnitude and width of OFD zones can change along fault strike. Within the OFD zones, the intensity of distributed displacement increases nonlinearly toward the main fault, as reflected in the density of faults, variance of block rotation, and the amount of displacement. Most of this displacement occurs within 100–200 m of the fault. Because similar displacement distributions are observed in studies of coseismic surface ruptures, it is probable that distributed displacement accumulates through multiple seismic events. If OFD progressively accumulates through time, then fault displacements and slip rates may be significantly underestimated where based on narrow aperture of piercing points (<100–200 m from the fault) as common in studies of Quaternary slip rates based on offset stream channels. Overall, ignoring distributed displacement may cause significant errors in geodynamic models.

[49] Structural accommodation of distributed displacement is observed to occur through a combination of block rotation and displacement along secondary faults subparallel to the main fault. Block rotation may be associated with upright folding adjacent to faults. In the context of a fault zone block model, we find that the increasing intensity of rotational displacement toward the main fault, as well as density of secondary faults, implies a decrease of block sizes toward the main fault. Where measurable, integrated strain in OFD zones is dominated by normal drag that adds to the overall displacement across the fault zone, though reverse drag may also be present where blocks interact and where steep slip gradients occur on faults. Distributed displacement measured from geology and damage zones measured from seismology and InSAR [*Cochran et al.*, 2009; *Fialko et al.*, 2002] seem to have a similar pattern, and extend to similar distances away from the main fault. This suggests that damage is distributed throughout the OFD zone via a network of secondary faults. Future studies may benefit from the study of the interaction between folding, distributed vertical axis rotation, and the extent of compliant zones. Such studies may shed light on the volume problem associated with block rotation and internal deformation of blocks.

Appendix A: Derivation of the Length Ratio of Secondary Faults to the Main Fault

[50] As shown in Figure 10c, the radius of circular blocks can be expressed as the height of the triangles defined by $L_{max} = mX$. The triangles HX_1E, FX_2G are isosceles right triangles due to the circular shape of the enclosing blocks. Thus, triangles HX_1E, FX_2G are also similar triangles and therefore the following ratios are equal for a pair of adjacent blocks (Figure 10c):

$$\frac{L_{max2}}{L_{max1}} = \frac{\overline{X_2G}}{\overline{X_1G}} = \frac{mX_2}{mX_1} = \frac{X_2}{X_1} = \frac{\overline{GF}}{\overline{EF}}. \tag{A1}$$

[51] The triangle EGF is also right triangle. The tangent of angle GEF is thus also equal to this set of ratios,

$$\frac{L_{max2}}{L_{max1}} = \frac{X_2}{X_1} = \frac{\overline{GF}}{\overline{EF}} = \tan(\angle GEF) = \tan\left(\frac{\pi}{4} + \theta\right), \tag{A2}$$

where $\theta = \tan^{-1}(m)$. Using the trigonometric identity for the tangent of a sum of two angles,

$$\tan(u + v) = \frac{\tan u + \tan v}{1 - \tan u \, \tan v}. \tag{A3}$$

[52] We find that the ratio of adjacent block lengths and distances to those blocks is a constant related to the slope of the line defining the relationship of block length to distance from the fault,

$$\frac{L_{max2}}{L_{max1}} = \frac{X_2}{X_1} = \frac{1+m}{1-m}. \tag{A4}$$

Multiplying the ratios for n adjacent blocks together, X_1 to X_n,

$$\frac{X_2}{X_1} \times \frac{X_3}{X_2} \times \frac{X_4}{X_3} \ldots \times \frac{X_n}{X_{n-1}} = \left(\frac{1+m}{1-m}\right)^{n-1}. \tag{A5}$$

Canceling X values that appear in both the numerator and denominator leaves

$$\frac{X_n}{X_1} = \left(\frac{1+m}{1-m}\right)^{n-1}. \tag{A6}$$

And solving for n,

$$n = \frac{\log(X_n/X_1)}{\log[(1+m)/(1-m)]} + 1. \tag{A7}$$

Starting at a minimum distance, X_1, equation (A7) is used to calculate the number of blocks required out to a distance W, the outer edge of the OFD zone. A finite minimum distance is also required. Otherwise an infinite number of blocks is needed. In order to get a conservative estimate of n, we use a minimum distance, X_0, of 1 m, which is the maximal width of fault gouge zone as described by *Chester*

et al. [2005]. Thus, X_1, the center of the closest block to the fault is

$$X_1 = \frac{X_0}{1-m} = \frac{1}{1-m}. \tag{A8}$$

[53] In a similar way, X_n can be defined from W as,

$$X_n = \frac{W}{1+m}. \tag{A9}$$

Thus, n represents the number of blocks bounded between 1 m from the fault to the outer edge of the OFD zone.

[54] With n we can then estimate the ratio between the summed lengths of secondary faults within OFD zone to the length of the adjacent main fault. We calculate the number of blocks of different radii, L_{max}, that can fit into a swath defined by the diameter of the largest block. R represents the radius of largest block at the edge of the OFD zone and r is a variable that represents the radius of the smaller blocks. K is the number of circles of radius r that can fit in the largest circle with radius R, and thus R = Kr or

$$2\pi R = 2\pi Kr. \tag{A10}$$

Thus, the cumulative circumference of circles of radius r that fit side by side into the diameter of the largest circle of radius R is the simply equal to the circumference of the largest circle. Within a swath defined by the diameter of the largest block (Figure 10c), the cumulative circumference of circular blocks, L_c is

$$L_c = 2n\pi R. \tag{A11}$$

[55] The length of the adjacent portion of the main fault is by definition 2R. Therefore the ratio of main fault length to secondary fault length, i.e., the secondary fault density,

$$\rho_f = \frac{L_c}{2R} = n\pi. \tag{A12}$$

References

Albers, J. P. (1967), Belt of sigmoidal bending and right-lateral faulting in the western Great Basin, *Geol. Soc. Am. Bull.*, *78*, 143–156, doi:10.1130/0016-7606(1967)78[143:BOSBAR]2.0.CO;2.

Baer, G., and Z. Reches (1991), Mechanics of emplacement and tectonic implications of the Ramon dike system, Israel, *J. Geophys. Res.*, *96*, 11,895–11,910, doi:10.1029/91JB00371.

Bartley, J. M., A. F. Glazner, and E. R. Schermer (1990), North-south contraction of the Mojave block and strike-slip tectonics in southern California, *Science*, *248*, 1398–1401, doi:10.1126/science.248.4961.1398.

Bartley, J. M., A. F. Glazner, J. M. Fletcher, M. E. Martin, and J. D. Walker (1992), Amount and nature of dextral off-set on neogene faults near Barstow, California, *Eos Trans. AGU*, *73*, 363.

Beck, M. E. (1976), Discordant paleomagnetic pole positions as evidence of regional shear in the western Cordillera of North America, *Am. J. Sci.*, *276*, 694–712.

Beck, M. E. (1980), Paleomagnetic record of plate-margin tectonic processes along the western edge of North America, *J. Geophys. Res.*, *85*, 7115–7131, doi:10.1029/JB085iB12p07115.

Bennett, R. A., B. P. Wernicke, N. A. Niemi, A. M. Friedrich, and J. L. Davis (2003), Contemporary strain rates in the northern Basin and Range province from GPS data, *Tectonics*, *22*(2), 1008, doi:10.1029/2001TC001355.

Brown, L. L., and M. P. Golombek (1985), Tectonic rotations within the Rio Grande Rift: Evidence from paleomagnetic studies, *J. Geophys. Res.*, *90*, 790–802, doi:10.1029/JB090iB01p00790.

Brune, J. N. (2001), Fault-normal dynamic unloading and loading: An explanation for "non-gouge" rock powder and lack of fault-parallel shear bands along the San Andreas fault, *EOS Trans. AGU*, *82*(47), Fall Meet. Suppl., abstract F854.

Chester, J. S., F. M. Chester, and A. K. Kronenberg (2005), Fracture surface energy of the Punchbowl Fault, San Andreas system, *Nature*, *437*, 133–136, doi:10.1038/nature03942.

Cochran, E. S., J. E. Vidale, and Y. G. Li (2003), Near-fault anisotropy following the Hector Mine earthquake, *J. Geophys. Res.*, *108*(B9), 2436, doi:10.1029/2002JB002352.

Cochran, E. S., Y. G. Li, P. M. Shearer, S. Barbot, Y. Fialko, and J. E. Vidale (2009), Seismic and geodetic evidence for extensive, long-lived fault damage zones, *Geology*, *37*, 315, doi:10.1130/G25306A.1.

Davis, G. H. (1984), *Structural Geology of rocks and Regions*, 592 pp., John Wiley, New York.

Demarest, H. H. (1983), Error analysis for the determination of tectonic rotation from paleomagnetic data, *J. Geophys. Res.*, *88*, 4321–4328, doi:10.1029/JB088iB05p04321.

Dennis, J. (1972), *Structural Geology*, 532 pp., John Wiley, New York.

Dibblee, T. W. (1964a), *Geological Map of the Ord Mountains Quadrangle, San Bernardino County, California, Miscellaneous Geologic Investigations Map I-427*, U.S. Geol. Surv., Washington, D. C.

Dibblee, T. W. (1964b), *Geological Map of the Rodman Mountains Quadrangle, San Bernardino County, California, Miscellaneous Geologic Investigations Map I-430*, U.S. Geol. Sur., Washington, D. C.

Dixon, T. H., S. Robaudo, J. Lee, and M. C. Reheis (1995), Constraints on present-day Basin and Range deformation from space geodesy, *Tectonics*, *14*, 755–772, doi:10.1029/95TC00931.

Dokka, R. K. (1983), Displacements on late Cenozoic strike-slip faults of the central Mojave Desert, *Calif. Geol.*, *11*, 305–308.

Dokka, R. K., and C. J. Travis (1990), Role of the Eastern California Shear Zone in accommodating Pacific-North American plate motion, *Geophys. Res. Lett.*, *17*, 1323–1326, doi:10.1029/GL017i009p01323.

Dor, O., Y. Ben-Zion, T. K. Rockwell, and J. Brune (2006), Pulverized rocks in the Mojave section of the San Andreas Fault Zone, *Earth Planet. Sci. Lett.*, *245*, 642–654, doi:10.1016/j.epsl.2006.03.034.

Faulkner, D. R., T. M. Mitchell, D. Healy, and M. J. Heap (2006), Slip on 'weak' faults by the rotation of regional stress in the fracture damage zone, *Nature*, *444*, 922–925, doi:10.1038/nature05353.

Fialko, Y. (2004), Probing the mechanical properties of seismically active crust with space geodesy: Study of the coseismic deformation due to the 1992 Mw 7.3 Landers (southern California) earthquake, *J. Geophys. Res.*, *109*, B03307, doi:10.1029/2003JB002756.

Fialko, Y., D. Sandwell, D. Agnew, M. Simons, P. Shearer, and B. Minster (2002), Deformation on nearby faults induced by the 1999 Hector Mine earthquake, *Science*, *297*, 1858–1862, doi:10.1126/science.1074671.

Fisher, R. A. (1953), Dispersion on a sphere, *Proc. R. Soc. London, Ser. A*, *217*, 295–305, doi:10.1098/rspa.1953.0064.

Fletcher, J. M., J. M. Bartley, M. W. Martin, A. F. Glazner, and D. J. Walker (1995), Large-magnitude continental extension: An example from the central Mojave metamorphic core complex, *Geol. Soc. Am. Bull.*, *107*, 1468–1483, doi:10.1130/0016-7606(1995)107<1468:LMCEAE>2.3.CO;2.

Fu, B., Y. Awata, J. Du, and W. He (2005), Late Quaternary systematic stream offsets caused by repeated large seismic events along the Kunlun fault, northern Tibet, *Geomorphology*, *71*, 278–292, doi:10.1016/j.geomorph.2005.03.001.

Gan, W., J. L. Svarc, J. C. Savage, and W. H. Prescott (2000), Strain accumulation across the Eastern California Shear Zone at latitude 36°30′N, *J. Geophys. Res.*, *105*, 16,229–16,236, doi:10.1029/2000JB900105.

Glazner, A. F., J. M. Bartley, and W. K. Sanner (2000), Nature of the southwestern boundary of the central Mojave Tertiary province, Rodman Mountains, California, *Geol. Soc. Am. Bull.*, *112*, 34–44, doi:10.1130/0016-7606(2000)112<34:NOTSBO>2.0.CO;2.

Glazner, A. F., D. J. Walker, J. M. Bartley, and J. M. Fletcher (2002), Cenozoic evolution of the Mojave block of southern California, in *Geologic evolution of the Mojave desert and Southwestern Basin and Range*, edited by A. F. Glazner et al., *Mem. Geol. Soc. Am.*, *195*, 19–41.

Greenhaus, M. R., and A. Cox (1979), Paleomagnetism of the Morro Rock-Islay Hill complex as evidence for crustal block rotations in central coastal California, *J. Geophys. Res.*, *84*, 2393–2400, doi:10.1029/JB084iB05p02393.

Haeussler, P. J., et al. (2004), Surface rupture and slip distribution of the Denali and Totschunda Faults in the 3 November 2002 M 7.9 Earthquake, Alaska, *Bull. Seismol. Soc. Am.*, *94*(6), 23–52.

Hart, E. W. (1988), Fault-rupture hazard zones in California, *Spec. Publ. 42*, Calif. Div. of Mines and Geol., Dept. of Conserv., Sacramento, Calif.

Hilley, G. E., R. Bürgmann, P. Molnar, and P. Zhang (2005), Bayesian inference of plastosphere viscosities near the Kunlun Fault, northern Tibet, *Geophys. Res. Lett.*, *32*, L01302, doi:10.1029/2004GL021658.

Howard, K. A., and D. M. Miller (1992), Late Cenozoic faulting at the boundary between the Mojave and Sonoran blocks: Bristol Lake area, California, in *Deformation associated with the Neogene eastern California shear zone, southwestern Arizona and southeastern California*, edited by S. M. Richard, p. 37–47, San Bernardino County Museum, Redlands, Calif.

Johnson, A. M., R. W. Fleming, and K. M. Cruikshank (1994), Shear zones formed along long, straight traces of fault zones during the 28 June 1992 Landers, California, earthquake, *Bull. Seismol. Soc. Am.*, *84*, 499–510.

Jones, C. H. (2002), User-driven integrated software lives: "PaleoMag" paleomagnetics analysis on the macintosh, *Comput. Geosci.*, *28*(10), 1145–1151, doi:10.1016/S0098-3004(02)00032-8.

Katz, O., Z. Reches, and G. Baer (2003), Faults and their associated host rock deformation: Structure of small faults in a quartz-syenite body, southern Israel, *J. Struct. Geol.*, *25*, 1675–1689, doi:10.1016/S0191-8141(03)00011-7.

Kimurah, H., Y. Itoh, and H. Tsutsumi (2004), Quaternary strike-slip crustal deformation around an active fault based on paleomagnetic analysis: A case study of the Enako fault in central Japan, *Earth Planet. Letters*, *226*, 321–334, doi:10.1016/j.epsl.2004.08.003.

Kirschvink, J. L. (1980), The least-squares line and plane and the analysis of paleomagnetic data, *Geophys. J. R. Astron. Soc.*, *62*, 699–718.

Lamb, S. H. (1987), A model for tectonic rotations about a vertical axis, *Earth Planet. Sci. Lett.*, *84*, 75–86, doi:10.1016/0012-821X(87)90178-6.

Lawson, A. C. (1908), The California Earthquake of April 18, 1906: Report of the State Earthquake Investigation Commission in two volumes and atlas, *Carnegie Inst. Washington Publ.*, *87*, 192 p.

Lemaitre, J., and R. Desmorat (2005), *Engineering Damage Mechanics: Ductile, Creep, Fatigue and Brittle Failures*, 400 pp., Springer, Berlin.

Li, Y. G., and J. E. Vidale (2001), Healing of the shallow fault zone from 1994–1998 after the 1992 M7.5 Landers, California, earthquake, *Geophys. Res. Lett.*, *28*, 2999–3002, doi:10.1029/2001GL012922.

Li, Y., J. Vidale, K. Aki, F. Xu, and T. Burdette (1998), Evidence of shallow fault zone strengthening after the 1992 M7.5 Landers, California, earthquake, *Science*, *279*, 217–219, doi:10.1126/science.279.5348.217.

Li, Y. G., J. E. Vidale, S. M. Day, and D. D. Oglesby (2002), Study of the 1999 M.7.1 Hector Mine, California, earthquake fault plane by trapped waves, *Bull. Seismol. Soc. Am.*, *92*(4), 1318–1332, doi:10.1785/0120000909.

Li, Y. G., J. E. Vidale, M. D. Steven, D. D. Oglesby, and E. Cochran (2003), Postseismic fault healing on the rupture zone of the 1999 M 7.1 Hector Mine, California, earthquake, *Bull. Seismol. Soc. Am.*, *93*, 854–869, doi:10.1785/0120020131.

Liu, J., Y. Klinger, K. Sieh, and C. Rubin (2004), Six similar sequential ruptures of the San Andreas fault, Carrizo Plain, California, *Geology*, *32*, 649–652, doi:10.1130/G20478.1.

McGill, S. M., and C. M. Rubin (1999), Surfical slip distribution on the central Emerson fault during the June 28, 1992 Landers earthquake, California, *J. Geophys. Res.*, *104*, 4811–4833, doi:10.1029/98JB01556.

Meade, B. J., and B. H. Hager (2005), Block models of crustal motion in southern California constrained by GPS measurements, *J. Geophys. Res.*, *110*, B03403, doi:10.1029/2004JB003209.

Michel, R., and J.-P. Avouac (2006), Coseismic surface deformation from air photos: The kickapoo stepover in the 1992 Landers rupture, *J. Geophys. Res.*, *111*, B03408, doi:10.1029/2005JB003776.

Miller, D. M., and J. C. Yount (2002), Late Cenozoic tectonic evolution of the north-central Mojave Desert inferred from fault history and physiographic evolution of the Fort Irwin area, California, in *Geologic Evolution of the Mojave Desert and Southwestern Basin and Range*, edited by A. F. Glazner, J. D. Walker, and J. M. Bartley, *Mem. Geol. Soc. Am.*, *195*, 173–197.

Miller, M. M., D. J. Johnson, T. H. Dixon, and R. K. Dokka (2001), Refined kinematics of the Eastern California shear zone from GPS observations, *J. Geophys. Res.*, *106*, 2245–2264, doi:10.1029/2000JB900328.

Nelson, M. R., and C. H. Jones (1987), Paleomagnetism and crustal rotations along a shear zone, Las Vegas Range, southern Nevada, *Tectonics*, *6*, 13–33, doi:10.1029/TC006i001p00013.

Nielson, J. E., D. R. Lux, G. B. Dalrymple, and A. F. Glazner (1990), Age of Peach Springs Tuff, southern California and western Arizona, *J. Geophys. Res.*, *95*, 571–580, doi:10.1029/JB095iB01p00571.

Oskin, M., and A. Iriondo (2004), Large-magnitude transient strain accumulation on the Blackwater fault, Eastern California shear zone, *Geology*, *32*, 313–316, doi:10.1130/G20223.1.

Oskin, M. E., L. A. Perg, D. Blumentritt, S. Mukhopadhyay, and A. Iriondo (2007), Slip rate of the Calico fault: Implications for geologic versus geodetic discrepancy in the Eastern Califonia shear zone, *J. Geophys. Res.*, *112*, B03402, doi:10.1029/2006JB004451.

Oskin, M., L. Perg, E. Shelef, M. Strane, E. Gurney, B. Singer, and X. Zhang (2008), Elevated shear-zone loading rate during an earthquake cluster in eastern, *Calif. Geol.*, *36*(6), 507–510.

Passchier, C. W. (2001), Flanking structures, *J. Struct. Geol.*, *23*, 951–962, doi:10.1016/S0191-8141(00)00166-8.

Reches, Z., and A. Eidelman (1995), Drag along faults, *Tectonophysics*, *247*, 145–156, doi:10.1016/0040-1951(94)00170-E.

Rice, J. R., C. G. Sammis, and R. Parsons (2005), Off-fault secondary failure induced by a dynamic slip pulse, *Bull. Seismol. Soc. Am.*, *95*(1), 109–134, doi:10.1785/0120030166.

Richard, P., B. Mocquet, and P. R. Cobbold (1991), Experiments on simultaneous faulting and folding above a basement wrench fault, *Tectonophysics*, *188*, 133–141, doi:10.1016/0040-1951(91)90319-N.

Rockwell, T. K., and Y. Ben-Zion (2007), High localization of primary slip zones in large earthquakes from paleoseismic trenches: Observations and implications for earthquake physics, *J. Geophys. Res.*, *112*, B10304, doi:10.1029/2006JB004764.

Rockwell, T. K., S. Lindvall, M. Herzberg, D. Murbach, T. Dawson, and G. Berger (2000), Paleoseismology of the Johnson Valley, Kickapoo, and Homestead Valley faults: Clustering of earthquakes in the Eastern California Shear Zone, *Bull. Seismol. Soc. Am.*, *90*, 1200–1236, doi:10.1785/0119990023.

Rockwell, T. K., S. Lindvall, T. Dawson, R. Langridge, W. R. Lettis, and Y. Klinger (2002), Lateral offsets on surveyed cultural features resulting from the 1999 Izmit and Düzce Earthquakes, Turkey, *Bull. Seismol. Soc. Am.*, *92*, 79–94, doi:10.1785/0120000809.

Rymer, M. J., G. G. Seitz, K. D. Weaver, A. Orgil, G. Faneros, J. C. Hamilton, and C. Goetz (2002), Geologic and paleoseismic study of the Lavic Lake Fault at Lavic Lake Playa, Mojave Desert, southern California, *Bull. Seismol. Soc. Am.*, *92*, 1577–1591, doi:10.1785/0120000936.

Salyards, S. L., K. E. Sieh, and J. L. Kirschvink (1992), Paleomagnetic measurement of nonbrittle coseismic deformation across the San Andreas fault at Pallett Creek, *J. Geophys. Res.*, *97*, 12,457–12,470, doi:10.1029/92JB00194.

Scholz, C. H., N. H. Dawers, J. Z. Yu, M. H. Anders, and P. A. Cowie (1993), Fault growth and fault scaling laws: Preliminary results, *J. Geophys. Res.*, *98*, 21,951–21,961, doi:10.1029/93JB01008.

Schouten, H., K. D. Klitgord, and D. G. Gallo (1993), Edge-driven microplate kinematics, *J. Geophys. Res.*, *98*, 6689–6701.

Shipton, Z. K., J. P. Evans, R. E. Abercrombie, and E. E. Brodsky (2006), The missing sinks: Slip localization in faults, damage zones, and the seismic energy budget, in *Earthquakes: Radiated Energy and the Physics of Faulting, Geophys. Monogr. Ser.*, vol. 170, edited by R. Abercrombie et al., p 217–222, AGU, Washington, D. C.

Sieh, K. E., and R. H. Jahns (1984), Holocene activity of the San Andreas fault at Wallace Creek, California, *Bull. Geol. Soc. Am.*, *95*(8), 883–896, doi:10.1130/0016-7606(1984)95<883:HAOTSA>2.0.CO;2.

Sonder, L. J., C. H. Jones, S. L. Salyards, and K. M. Murphy (1994), Vertical axis rotations in the Las Vegas Valley Shear Zone, southern Nevada: Paleomagnetic constraints on kinematics and dynamics of block rotations, *Tectonics*, *13*, 769–788, doi:10.1029/94TC00352.

Strane, M. (2007), Slip rate and structure of the nascent Lenwood fault zone, eastern California, 55 pp., Masters, Univ. of North Carolina, Chapel Hill, N. C.

Thatcher, W., and M. Lisowski (1987), Long-term seismic potential of the San Andreas fault southeast of San Francisco, California, *J. Geophys. Res.*, *92*, 4771–4784, doi:10.1029/JB092iB06p04771.

Treiman, J. A., K. J. Kendrick, W. A. Bryant, T. K. Rockwell, and S. F. McGill (2002), Primary surface rupture associated with the Mw 7.1 16 October 1999 Hector Mine earthquake, San Bernardino County,

California, *Bull. Seismol. Soc. Am.*, *92*, 1171–1191, doi:10.1785/0120000923.

Valentine, M. J., L. L. Vbrown, and M. P. Golombek (1993), Cenozoic crustal rotations in the Mojave Desert from paleomagnetic studies around Barstow, California, *Tectonics*, *12*, 666–677, doi:10.1029/92TC02813.

Van der Woerd, J., F. J. Ryerson, P. Tapponnier, Y. Gaudemer, R. Finkel, A. S. Meriaux, M. Caffee, Z. Guoguang, and H. Qunlu (1998), Holocene left-slip rate determined by cosmogenic surface dating on the Xidatan segment of the Kunlun fault (Qinghai, China), *Geology*, *26*, 695–698, doi:10.1130/0091-7613(1998)026<0695:HLSRDB>2.3.CO;2.

Vermilye, J. M., and C. H. Scholz (1998), The process zone: A microstructural view of fault growth, *J. Geophys. Res.*, *103*, 12,223–12,237, doi:10.1029/98JB00957.

Wells, R. E., and J. W. Hillhouse (1989), Paleomagnetism and tectonic rotation of the lower Miocene Peach Springs Tuff: Colorado Plateau, Arizona, to Barstow California, *Geol. Soc. Am. Bull.*, *101*, 846–863, doi:10.1130/0016-7606(1989)101<0846:PATROT>2.3.CO;2.

Wilbur, C. (1980), The nature and origin of Quaternary basaltic volcanism in the central Mojave desert area, California, Ms thesis, 134 p., San Jose State Univ., San Jose, Calif.

Wilson, B., T. Dewers, Z. Reches, and J. Brune (2005), Particle size and energetics of gouge from earthquake rupture zones, *Nature*, *434*, 749–752, doi:10.1038/nature03433.

Yamashita, T. (2000), Generation of microcracks by dynamic shear rupture and its effects on rupture growth and elastic wave radiation, *Geophys. J. Int.*, *143*, 395–406, doi:10.1046/j.1365-246X.2000.01238.x.

Zoback, M. D., et al. (1987) New evidence on the state of stress of the San Andreas fault system, *Science*, *238*, 1105–1111.

M. Oskin, Department of Geology, University of California, Davis, CA 95616, USA.

E. Shelef, Department of Geological and Environmental Sciences, Stanford University, Stanford, CA 94305, USA. (shelef@stanford.edu)